Low-Speed CFD Simulations of High-Speed Wing Configurations for a Highly Maneuverable UAV

Undergraduate Honors Thesis

Presented in Partial Fulfillment of the Requirements for the Degree of Bachelor of Science with Honors Research Distinction at The Ohio State University

By

Caleb Jordan Rajasuriyar

Undergraduate Program in Mechanical Engineering

The Ohio State University

2024

Undergraduate Thesis Committee

Dr. Clifford Whitfield, Advisor

Dr. Matthew McCrink

Abstract

In the past few decades, unmanned aerial vehicles have become ever more present in the skies above. This can be attributed to key advancements in control systems, navigation systems, communications hardware, and other key systems that were not readily available before. The use of unmanned aerial vehicles by the military is growing rapidly as their potential to fulfill various missions has been revealed through recent conflicts. The ability to send unmanned aerial vehicles into a combat zone without having to risk the lives of pilots is a capability that military aircraft of the past were not able to offer. This same technology is actively being assessed and used for non-defense applications as well, such as fighting forest fires, agricultural purposes, law enforcement applications, and more. With a technology that has so much potential and a continuously growing market, unmanned aerial vehicles are an important area to study to fully realize their potential.

The purpose of this research was to investigate the low-speed aerodynamics of high-speed wing configurations for an unmanned aerial vehicle (UAV) using Computational Fluid Dynamics (CFD). This project was motivated by the ongoing research and development of unmanned aerial vehicles at The Ohio State University Aerospace Research Center. The experimental UAV constructed for investigation met four different design requirements: (1) high speed, (2) highly maneuverable, (3)

aerodynamically interesting, and (4) multi-configurable. This research focuses on the low-speed aerodynamics of a novel UAV with a delta wing that has a 60-degree leading-edge sweep and rounded leading edges. Requirements (1) to (3) are fulfilled by using a delta wing configuration. The delta wing excels in the supersonic flow regime and can withstand much higher g-forces compared to other wing configurations. However, it underperforms in the subsonic flow regime, making it vital to study at low speeds to understand how its performance can be enhanced.

Computational analysis was done using Ansys FLUENT to develop a full aircraft model that characterized important flow features of the delta wing at various angles of attack. Simulations were conducted at standard day conditions and a Reynolds number of 5×10^5. Model results were verified using pressure, velocity, and streamline contours. The model was then validated by comparing the lift and drag coefficient results with experimental and theoretical data. It was revealed that at low speeds and high angles of attack leading edge vortices form, which aid the delta wing in generating additional lift in the subsonic flow regime. As the angle of attack increases, the vortices grow spanwise and begin to break down resulting in a loss of lift. The results from this research will complement existing wind tunnel results and aid in future design improvements by the FVDT to the experimental UAV. Furthermore, results from this research will help aid those in industry and the Department of Defense (DOD) in the design of unmanned aerial vehicles.

Acknowledgments

First and foremost, I would like to thank my research advisor Professor Clifford Whitfield. His mentorship and support have been a great supplement to my undergraduate studies. Through my research experience, I have learned a significant amount about aircraft design and gained valuable industry skills that I will translate to my future graduate school and industry careers. I am grateful for the trust he has put in me and for allowing me to do work that will help those in industry, government, and our lab.

Second, I would like to thank the other students at the Aerospace Research Center (ARC) that I collaborated with on this project. Specifically, I would like to give a special thank you to Ph.D. students Colin Trussa and Anthony Pisano. This research would not have been possible without their guidance and technical knowledge.

Finally, I would like to thank my family and friends for their unwavering love and support. Throughout my life, they have stood by my side through the good times and the bad. Their encouragement and guidance have helped me to pursue my dreams and accomplish my goals. This journey up until this point would not have been possible without their support and for that, I will be forever grateful.

Table of Contents

List of Figures

Chapter 1. Introduction

1.1 Background

With the rapid technological advancements in the past few decades, the use of unmanned aerial vehicles by civilians, law enforcement agencies, and the United States military has grown dramatically in recent times. As defined by the DOD, UAVs are aerial vehicles that do not carry a pilot, use aerodynamic forces to provide vehicle lift, can fly autonomously or be piloted remotely, can be expendable or recoverable, and carry a lethal or non-lethal payload [1]. UAVs have been widely used by the United States military throughout past conflicts and the global war on terror. They have been used in various roles, such as intelligence, surveillance, and reconnaissance (ISR); close air support (CAS); and communications relay [2]. Some notable platforms that have met these operational roles include the MQ-9 Reaper, MQ-1 Predator, RQ-4 Global Hawk, and RQ-7 Shadow. These platforms and more can be seen below in Figure 1.

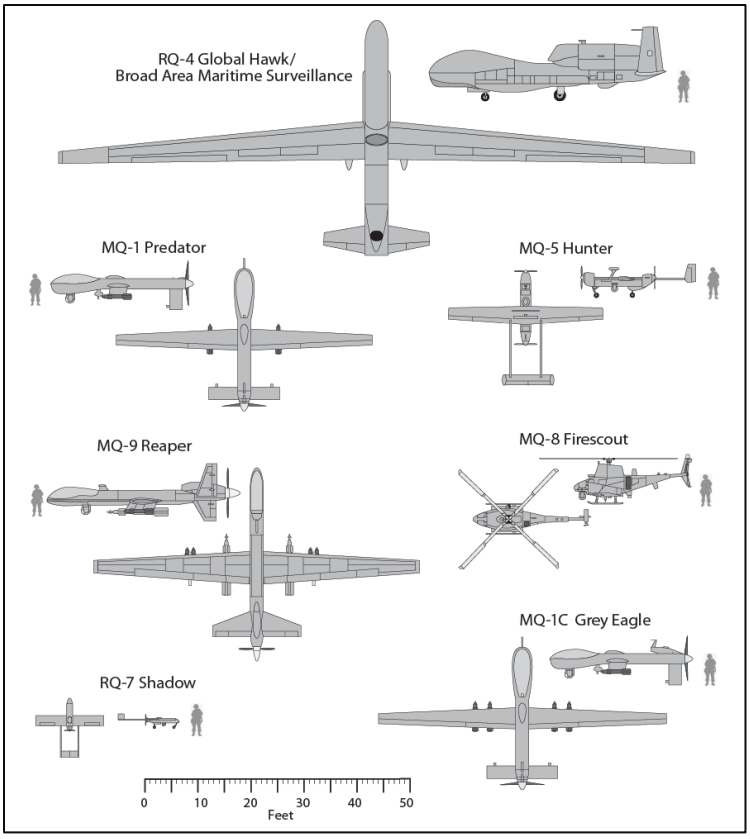

Figure 1. United States military unmanned aerial vehicles [1]

During Operation Iraqi Freedom (OIF), the Global Hawk was attributed with providing 55% of time sensitive targets generated to kill air defense equipment between 8 March 2003 and 23 April 2003 [3]. In 16 missions, the Global Hawk located 13 Surface-to-Air Missile (SAM) batteries, 50 SAM launchers, over 70 SAM transport vehicles, and over 300 tanks [3]. The critical intelligence that Global Hawk provided is just one example demonstrating how instrumental UAVs can be for military operations.

Although UAVs have been used mainly in just these roles, the DOD and analysts believe UAV systems can replace manned aircraft in various other roles. These include

aerial refueling; air-to-air combat; strategic bombing; battle management and command and control (BMC2); suppression and destruction of enemy air defenses; and electronic warfare (EW) [2]. One area of particular interest is the air-to-air combat role, which is a role that could be fulfilled by an uninhabited combat aerial vehicle (UCAV). In March 2003, it was reported that a Predator launched a Stinger air-to-air missile at an Iraqi MiG before the Iraqi MiG shot it down [1]. Although the Predator was lost, this was a small step in moving towards an air-to-air combat-capable UAV. Currently, programs like Boeings Loyal Wingman and the U.S. Air Forces Skyborg program are actively looking at developing air combat capabilities for UAVs [2]. For this to be achieved, many obstacles need to be overcome first. These obstacles include the vulnerabilities UAVs face to air defense systems and enemy fighter aircraft. One way to improve their survivability is by improving their maneuverability using a delta wing.

With the growing need for more highly maneuverable UAVs, the Flight Vehicle Design and Testing Group (FVDT) at the ARC is experimenting with a novel UAV that utilizes a delta wing configuration. The unique aircraft was designed to meet four different design requirements: high speed, highly maneuverable, aerodynamically interesting, and multi-configurable. The baseline aircraft design includes an axisymmetric fuselage, a single vertical tail, and a delta wing configuration. The delta wing being used has a 60-degree leading-edge sweep and a high-speed symmetric airfoil with rounded leading edges. The use of the delta wing satisfied all four key design requirements. To study the aerodynamic performance of the delta wing at subsonic speeds, the FVDT

performed experimental testing and computational analysis. The computational analysis and results will be discussed in Chapters 2 and 3 respectively.

1.1.1 Delta Wing

The delta wing is a special type of swept wing that has become widely used on various aircraft, ranging from civilian airliners to military aircraft. The basic design of a delta wing is a triangular swept wing that enables aircraft to perform high g maneuvers, carry increased payloads, and have a lighter-weight wing structure. Due to its desirable aerodynamic performance characteristics at supersonic speeds, the delta wing is used by a variety of military aircraft designs. Military aircraft, such as fighter jets, are required to be able to perform high-g maneuvers, dogfight, and deliver a payload to a target with precision. Two types of air combat situations fighter jets may find themselves in are short and medium-range air combat.

According to Herbst [4], short-range air combat is characterized by low speeds, high maneuverability, and a fluctuation of total energy. On the other hand, medium-range air combat is characterized by supersonic speeds, careful energy management, and constant total energy. The aircraft focused on in this research falls into the first category defined by Herbst. The delta wing and its variants demonstrate good short and medium-range capabilities, which is one reason why it is so prevalent amongst military aircraft. Some of the most notable military aircraft to use the delta wing and its several variants are the Mig-21, SR-71, F-22, Dassault Rafale, and Eurofighter Typhoon. Below in Figure 2, the SR-71 Blackbird, a strategic reconnaissance aircraft, is shown.

Figure 2. Lockheed Martin SR-71 Blackbird

The SR-71 Blackbird was a Mach 3+, high-altitude, reconnaissance aircraft that utilized a variant of the delta wing known as the swept double delta. Even though delta-wing aircraft are high-speed vehicles, like the SR-71, there are various instances when they need to travel at low speeds [5]. Due to this and the delta wing's wide use, it is imperative to understand its aerodynamic performance at low speeds.

Although the delta wing excels in the supersonic flow regime, the delta wing does not perform as well in the subsonic flow regime. One area that the delta wing underperforms in is generating lift at low speeds. To maintain lift in the subsonic flow regime, a special phenomenon called the leading-edge vortex (LEV) occurs at high angles of attack. By better understanding this phenomenon and the other aerodynamic

characteristics of the delta wing at subsonic speeds, the performance and maneuverability of an aircraft can be improved. The following sections will focus on different aspects of the delta wings aerodynamics at subsonic speeds, which led to the motivation and objectives of this research.

1.1.2 Leading Edge Vortex

A key feature of the delta wing at low speeds and high angles of attack is the leading-edge vortex. It is one of the key features that contribute to the non-linear aerodynamic characteristics of the delta wing. In the subsonic flow regime, the vortex plays an important role because it is the primary lifting force for delta wings. The vortex adds an additional lift component that drastically increases the stall angle of attack of the aircraft compared to conventional low-swept wings [6]. Below in Figure 3, the leading-edge vortex formation is shown.

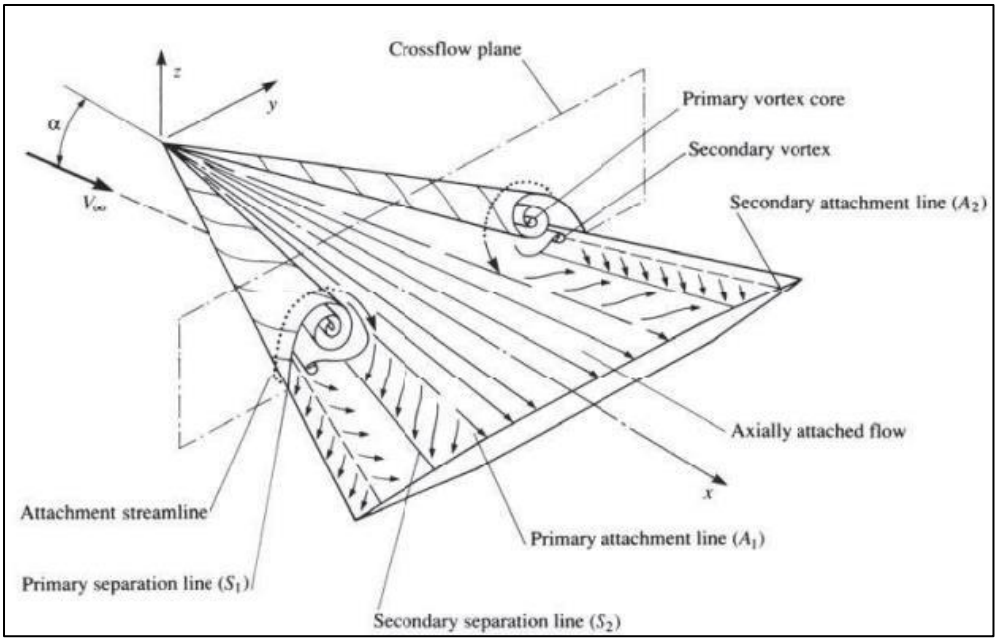

Figure 3. Leading edge vortex formation [5]

As can be seen above, the primary leading edge vortex forms around the highly swept leading edges of the delta wing due to boundary layer flow separation. More specifically, the leading-edge vortex is a combination of discrete vortices shedding off the leading edge that form a primary vortex [6]. The mechanism that results in these vortex formations is a pressure difference between the top and bottom surfaces. The pressure on the bottom of the wing at an angle of attack is higher than the pressure on the top surface, which results in the flow on the bottom trying to curl around the leading edge to the top [5]. When the primary vortex is fully formed, it interacts with the boundary layer on the surface of the wing, resulting in further boundary layer separation. This further separation results in the formation of a second counter-rotating vortex to form just

underneath the primary vortex. The mechanism that results in the formation of this second counter-rotating vortex is a large lateral pressure gradient at the primary reattachment line of the primary vortex. The boundary layer on the surface of the wing inboard of the primary reattachment line separates and rolls up into the secondary rotating vortex [6].

These vortices are sources of high energy and high vorticity flow, which result in regions characterized by small local static pressure [5]. This results in the surface pressure near the leading edges on the top of the wing being much lower than along the middle of the wing. Furthermore, the surface pressure near the leading edges is far lower than the freestream pressure. On the bottom side of the wing, the surface pressure remains constant spanwise [5]. The leading-edge vortices create a strong suction effect on the top surface of the wing, resulting in enhanced lift. This can be clearly seen below in Figure 5, where the arrows represent the suction effect of the leading-edge vortices.

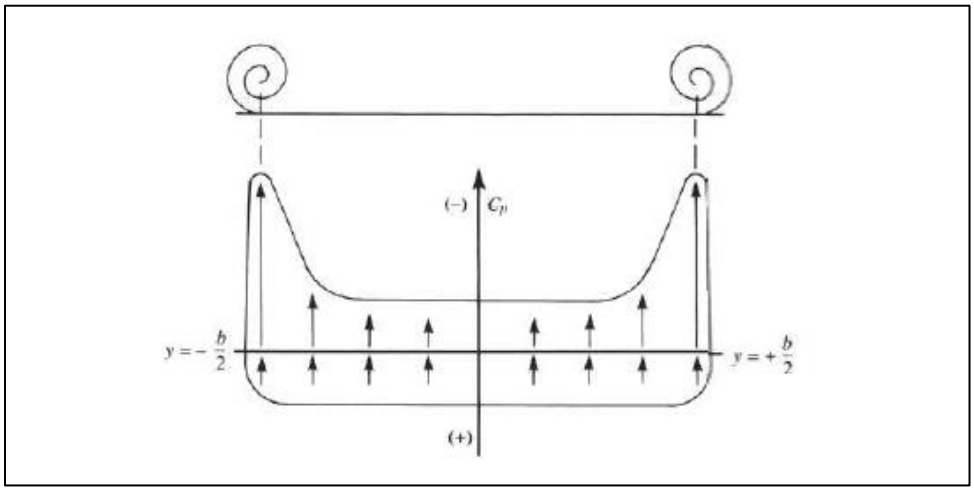

Figure 4. Spanwise pressure coefficient distribution along a delta wing [5]

Understanding the effects of the leading-edge vortex is vital for improving the performance of any aircraft design looking to utilize this wing configuration. Another key feature that is important to study is how these vortices break down.

1.1.3 Vortex Breakdown

Vortex breakdown, also known as vortex bursting, is a common flow feature that is exhibited by delta wings at high angles of attack. The mechanism that results in this phenomenon is a rapid decrease in axial flow that causes the leading-edge vortices to expand and decay into turbulence [6]. Vortex breakdown has been a subject of great interest since the early 1950s when aircraft designs started incorporating the delta wing. Various experiments have been conducted in wind and water tunnels to better understand this phenomenon. Through these experiments, various types of vortex breakdowns have been identified, but the two most exhibited by delta wings are the bubble and spiral types. Below in Figure 5, the common types of vortex breakdown are shown.

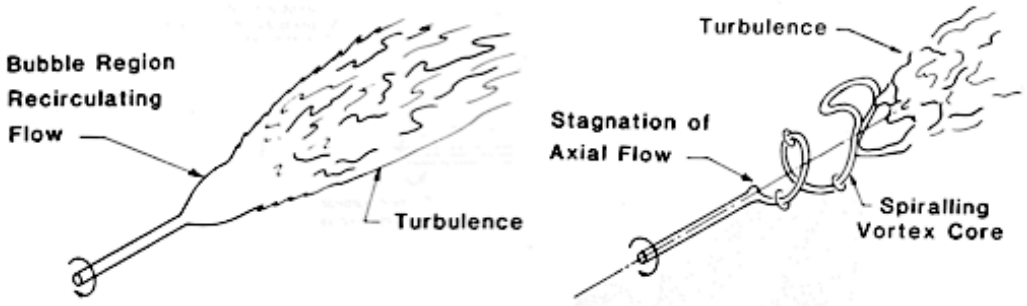

a. Bubble b. Spiral

Figure 5. Common types of vortex breakdown [7]

In Figure 5a, the bubble or "axisymmetric" mode of breakdown is characterized by a stagnation point in the axis of the vortex, followed by an oval-shaped recirculation bubble, which then transitions into turbulence [7]. In Figure 5b, the spiral mode of breakdown is characterized by rapid deceleration of airflow by an abrupt kink, which results in the flow taking the form of a spiral that transitions into turbulence after one or two spirals [7]. Of these two types of vortex breakdown modes, the delta wing exhibits spiral vortex breakdown more than bubble vortex breakdown. According to Gursul [8], vortex breakdown can be attributed to two important parameters: swirl level and external pressure gradient outside the vortex core. An increase in either parameter can result in vortex breakdown occurring prematurely. For leading-edge vortices, both parameters are heavily dependent on wing geometry, such as the sweep angle of the wing.

Another type of vortex bursting exhibited by delta wings that is important to understand is wing rock. Wing rock is described as a limited oscillation phenomenon occurring during high-angle attack maneuvers when the aircraft is rolling [9]. Various reasons have been postulated for why wing rock occurs in delta-winged aircraft. One of these reasons is attributed to the non-linearities in static rolling and yawing moments at high angles of attack [9]. This can have a negative impact on the performance of fighter aircraft that will perform such maneuvers due to the instability it could cause.

1.2 Motivation

The delta wing provides engineers with a unique wing configuration that offers various aerodynamic capabilities but also presents new challenges that need to be overcome. Whether a subsonic glider or supersonic fighter jet, all aircraft must take off and land at subsonic speeds. The subsonic flow regime is where the delta wing experiences many of these challenges. This makes it imperative to understand the aerodynamic performance of the delta wing at low speeds when designing an aircraft. Developing a CFD model for the UAV with a delta wing and other high-speed wing configurations will aid the FVDT in making future performance improvements to the aircraft. Furthermore, results from these CFD simulations will be used to complement the experimental testing results that have been obtained. This research will also help further develop CFD applications as an aircraft design and analysis tool. In addition, with limited CFD data and information at low speeds and high angles of attack for the delta wing, this research will provide valuable insight into its performance in such conditions.

Another area results from this research will be directly applicable to is DOD applications. With a lack of highly maneuverable UAVs in the U.S. military inventory, this research can demonstrate how effective delta wings can be for UAVs in terms of improving aerodynamic performance. In addition, it could be directly applied to programs like the Air Forces Next Generation Air Dominance program, which is looking to develop a 6^{th} generation fighter jet and unmanned combat aerial vehicles to support it. The Air Force wants these UCAVs to be able to carry out missions in high-threat areas

that would be otherwise too dangerous for manned aircraft to go. For this to be possible, UCAVs that are highly maneuverable will be quintessential for mission success. Highly maneuverable UAVs will not only benefit military operations but will also avoid having to put pilot lives at risk.

1.3 Objectives

The primary goal of this research is to model the XQ-1A experimental drone with a 60-degree delta wing in Ansys FLUENT and validate the model using experimental and theoretical data. Once the model is validated, it will be modified to accommodate various high-speed wing configurations, such as the double delta, ogive, and diamond wing. These wing configurations will then be studied to predict their aerodynamic performance at low speeds and high angles of attack. After this is accomplished, the results obtained from the CFD model will be analyzed and compared to experimental and theoretical data to judge its accuracy. The results from this research will give the FVDT better insight into each wing configuration's unique aerodynamic characteristics and help make further design improvements to the UAV.

1.4 Outline

The remainder of this thesis is outlined as follows: Chapter 2 goes over the computational tools utilized, the aircraft geometry, and the computational set up. The computational set up includes mesh and fluid domain generation, model selection and

description, and boundary conditions. Chapter 3 presents the flow visualizations and the numerical results for each model. In addition, the model validation and verification process are discussed. Finally, Chapter 4 concludes the thesis with a summary of the work, discussion of major findings, and a discussion of future work.

Chapter 2. Computational Tools and Setup

2.1 Computational Tools

Computational Fluid Dynamics (CFD) is a branch of fluid mechanics that involves numerical methods to solve fluid flow problems. It is used in a wide variety of industries and can be applied to various problems. These include aerodynamic analysis, turbomachinery, HVAC, heat transfer, and more. Before computers, the only way for engineers to test and optimize their designs was through physical testing of a prototype. However, with the rise of computers and their computational power, CFD applications have become more widely used. Some of the applications used in industry include Ansys FLUENT, COMSOL Multiphysics, OPENFOAM, and Star-CCM+. Although CFD can be a beneficial tool in the aircraft design process, it has its limitations. It can be computationally expensive and time consuming when running simulations involving complex geometries and flow physics. In addition, inaccurate results due to many sources of errors are common, which is why experimental results are needed to validate such models. For this research, the aircraft model was analyzed using the student version of Ansys FLUENT due to it is ease of use and ability to handle complex geometries.

2.1.1 Ansys FLUENT

Ansys FLUENT is one of the most widely used CFD applications in industry and is known for its advanced physics modeling capabilities and accurate simulations. Most CFD tools, commercial or open source, use a mathematical model and numerical method to predict desired flow physics [10]. In CFD analysis, fluid flow and its associated properties, such as velocity, pressure, viscosity, density, and temperature, are all calculated based on defined operating conditions [10]. For all flows, Ansys FLUENT solves conservation equations for momentum and mass simultaneously [11]. These equations can be seen below in their general form. Equations 1 and 2 are known as the Navier-Stokes and Continuity equations respectively.

$$\frac{\partial}{\partial t}(\rho\,\vec{v}) + \nabla\cdot(\rho\vec{v}\vec{v}) = -\nabla p + \nabla\cdot(\bar{\bar{\tau}}) + \rho\vec{g} \qquad (1)$$

$$\frac{D\rho}{Dt} + \rho(\nabla\cdot\vec{v}) = 0 \qquad (2)$$

Additional equations will be solved for depending on the type of model and physics trying to be simulated. These equations are then solved on a meshed fluid domain using a finite volume method. The CFD solver in FLUENT solves the governing equations for unknown variables such as velocity and temperature at the centroid of each cell. Once the solution has converged, the results from these simulations can be post-processed to help engineers make informed decisions about designs. Various types of contours displaying important information can be created and the flow can be visualized.

Furthermore, FLUENT allows engineers to easily modify parameters of interest, which is critical for design optimization.

2.2 Aircraft Geometry

For this research, a novel UAV was developed by the Flight Vehicle Design and Testing Group that met four different design requirements as stated in Chapter 1. Designated as the XQ-1A, the UAV design incorporates area-ruling techniques to reduce high-speed compressible wave drag. Furthermore, the fuselage design allows for the incorporation of various wing configurations for experimental testing. The baseline model uses a 60-degree swept delta wing with a NACA 64-006 series airfoil. A 60-degree leading edge sweep was selected due to the extensive research done by the aerospace community on this wing sweep. This provides an established baseline for future research and development to be carried out. Below in Figure 6, the XQ-1A can be seen.

Figure 6. XQ-1A unmanned aerial vehicle

The delta wing was designed with a mean aerodynamic chord (mac) length of 1.17 ft, a wingspan of 2.08 ft, and a wing area of 1.83 sq-ft. For computational analysis, these same geometric characteristics were utilized to create a CAD model of the XQ-1A. Designed by Colin Trussa in SOLIDWORKS, the CAD model can be seen below in Figure 7. Geometric cleanup was not needed prior to the computational analysis due to there being no intersecting parts or small features that would impact the flow.

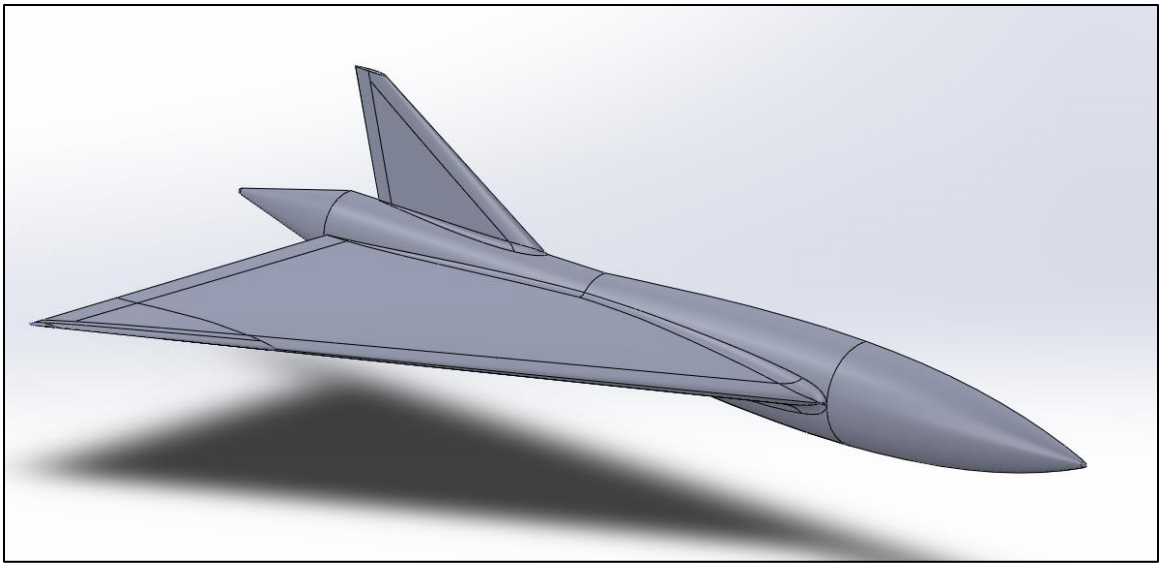

Figure 7. XQ-1A half model in SOLIDWORKS

2.3 Computational Setup

At subsonic speeds, delta wing aircraft are expected to fly at high angles of attack to maintain lift. It is in these conditions where complex flow features such as the leading-edge vortex develop. It is imperative to study these aerodynamic features of the delta wing experimentally and computationally to fully understand their effects on aircraft performance. For this research, 2D and 3D CFD models were developed for aerodynamic analysis. These models include the NACA 0012 and NACA 64-006 airfoils, a flat plate delta wing, and the XQ-1A UAV. For the NACA 0012 model, simulations were run using standard day conditions and a Reynolds number of 3×10^6. For the NACA 64-006 model, simulations were run using standard day conditions and a Reynolds number of 5×10^5 and 3×10^6. For the flat plate delta wing and XQ-1A models, simulations were

run using standard day conditions and a Reynolds number of 5×10^5. In this section, mesh and fluid domain generation will be discussed for each computational model that was developed. Furthermore, model selection and the boundary conditions used for each model will be discussed.

2.3.1 Mesh and Fluid Domain Generation

One of the most crucial and time intensive steps in CFD modeling is the mesh and fluid domain generation. Various considerations need to be considered during this process, such as the size of the fluid domain, type of mesh and cells to use, first boundary layer height, and the quality of the mesh. All these different parameters can have a massive impact on the accuracy and convergence of CFD simulation results. For external flow problems, it is important that the fluid domain be designed in such a way that the perturbations created by the presence of the body do not affect the boundaries [12]. If the domain is too small, the perturbations may not have enough time to reach an equilibrium state at the boundaries. This could result in the numerical boundary conditions affecting the flow around the body in a non-physical way and effect the accuracy of simulation results [12]. In general, for external flow problems involving airfoils and aircraft geometry, it is best practice to make the domain at least 10 chord lengths in all directions. Different fluid domain geometries can be selected for the type of problem being modeled. Two of the most common for external flow problems are a box and cylinder. The box shape is useful for simulating an airplane in ground effect or the interaction of a car with

a moving road [12]. The cylinder shape is useful for freestream analysis of an axisymmetric body or streamline geometry, such as a fighter aircraft [12].

For this research, 2D and 3D CFD simulations were run using a fluid domain geometry consisting of a semi-circle for the upstream portion and a rectangle for the downstream portion. For the 2D models of the NACA 0012 and NACA 64-006 airfoils, a semi-circle of radius 3.60 m and a rectangle of length 3.60 m was used. These dimensions were selected due to them being 10 times the chord length of the airfoil. Furthermore, the fluid domain was divided into four quadrants to simplify the meshing process. The fluid domain geometry for both these models can be seen below in Figure 8.

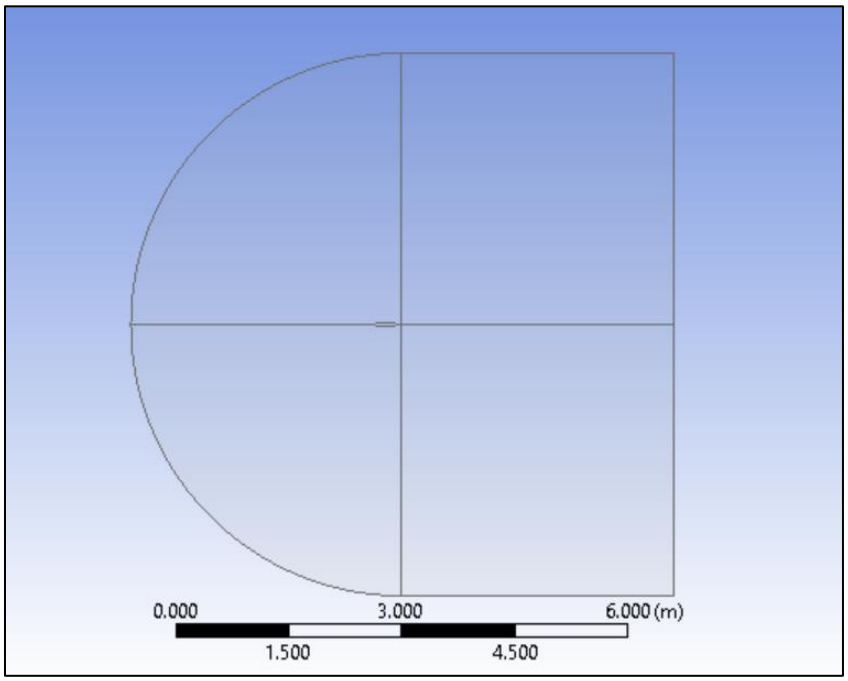

Figure 8. Fluid domain geometry for the NACA 0012 and NACA 64-006 models

For the 3D simulations of the flat plate delta and XQ-1A UAV similar geometric dimensions were utilized. For the flat plate delta wing, a semi-circle of radius 7.95 m, a rectangle of length 7.95 m, and a width of 5.30 m was used for the fluid domain geometry. The radius and length were 15 times the mean aerodynamic chord length, while the width was 10 times the mean aerodynamic chord length. Due to a strong lateral pressure gradient and the complexity of the leading-edge vortex, these dimensions were selected to ensure the flow around the wing would not be affected by the boundaries. Likewise, for the XQ-1A model, the fluid domain geometry was selected to be a semi-circle of radius 3.13182 m, a rectangle of length 3.13182 m, and a width of 3.13182 m. These dimensions were all 10 times the mac length. Below in Figure 9, the fluid domain geometry for the flat plate delta and XQ-1A can be seen.

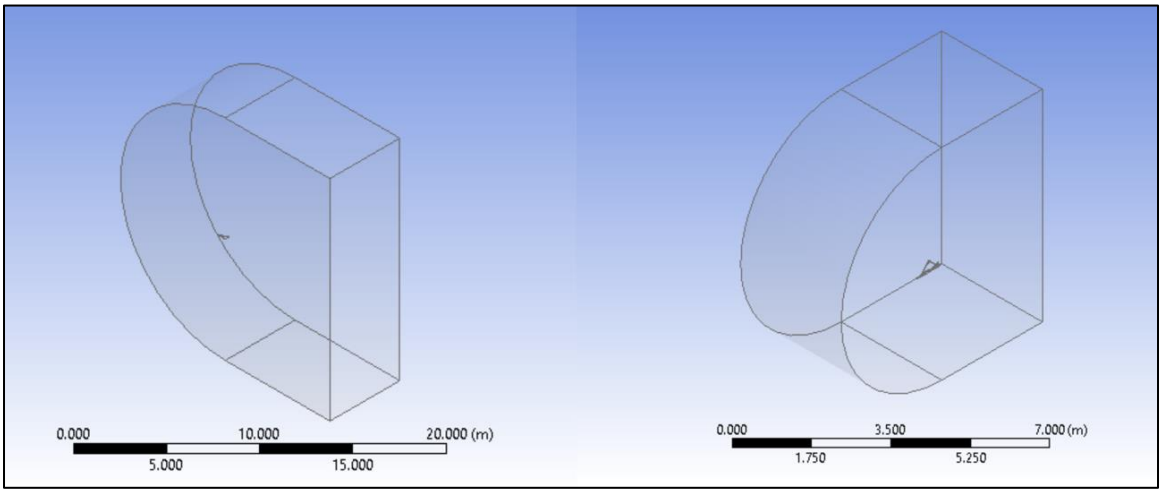

Figure 9. Fluid domain for a flat plate delta wing (left) and the XQ-1A UAV (right)

Once the fluid domain geometry is created and geometry clean-up has been performed, the model is ready to be meshed. One of the first considerations to make when meshing is deciding whether to use a structured or unstructured mesh. A structured mesh consists of cells arranged in an orderly manner. The benefits of a structured mesh include easier storage due to them requiring less data, high accuracy and low numerical error, and smooth transitions between elements. However, generating a structured mesh for complex geometry can be time consuming and sometimes not feasible. Furthermore, they tend to be computationally expensive due to them needing more cells to capture finer details in local regions. Due to this, an unstructured mesh may be favored over a structured mesh. An unstructured mesh is more general and can take the shape of any type of geometry. Due to their adaptability, they can utilize various cell types and have multiple cell types coexist in one mesh [13]. This ability allows unstructured meshes to be able to fit the geometry better and have better quality cells [13].

The types of cells that can be used in these meshes vary from 2D to 3D cases. The cell types offered by Ansys FLUENT for each case can be seen below in Figure 10.

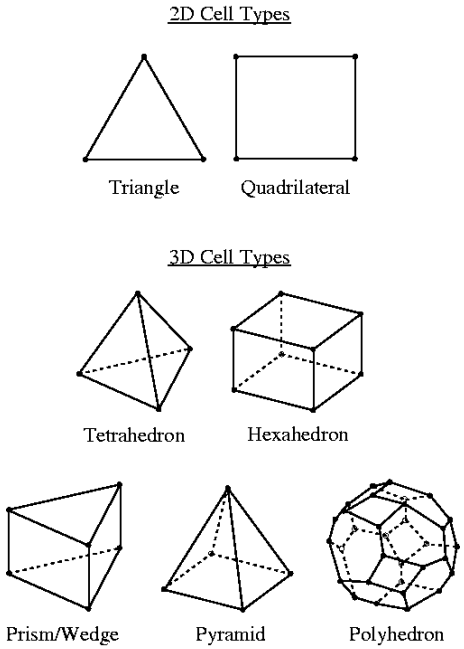

Figure 10. Cell types offered in Ansys FLUENT [11]

Structured meshes tend to use quadrilateral cells in 2D and hexahedra in 3D. Unstructured meshes use triangles in 2D and a variety of different cell types in 3D. Each cell type has its own benefits and drawbacks. For 3D models, a combination of polyhedral and hexahedral cells for the volume mesh is a good choice. This is known as a poly-hex core mesh and it offers robust convergence to lower residuals (i.e., 1e-6), faster convergence, and lower cell count. The need for fewer cells reduces the computational cost, which helps reduce simulation time.

For turbulent flow problems, it is important during the mesh generation process to resolve the boundary layer and other complex flow features. Turbulent flow is characterized by large gradients and rapid fluctuations in the mean flow and shear layers

with large shear strains. To accurately resolve the boundary layer, a non-dimensional number called the y^+ value is used. The y^+ value measures the first cell height needed near the wall. It is associated with the concept of the logarithmic "Law of the Wall". The "Law of the Wall" states that the average velocity of a turbulent flow at a certain point is equivalent to the logarithmic distance from that point to the wall. The "Law of the Wall" can be seen below in Figure 11.

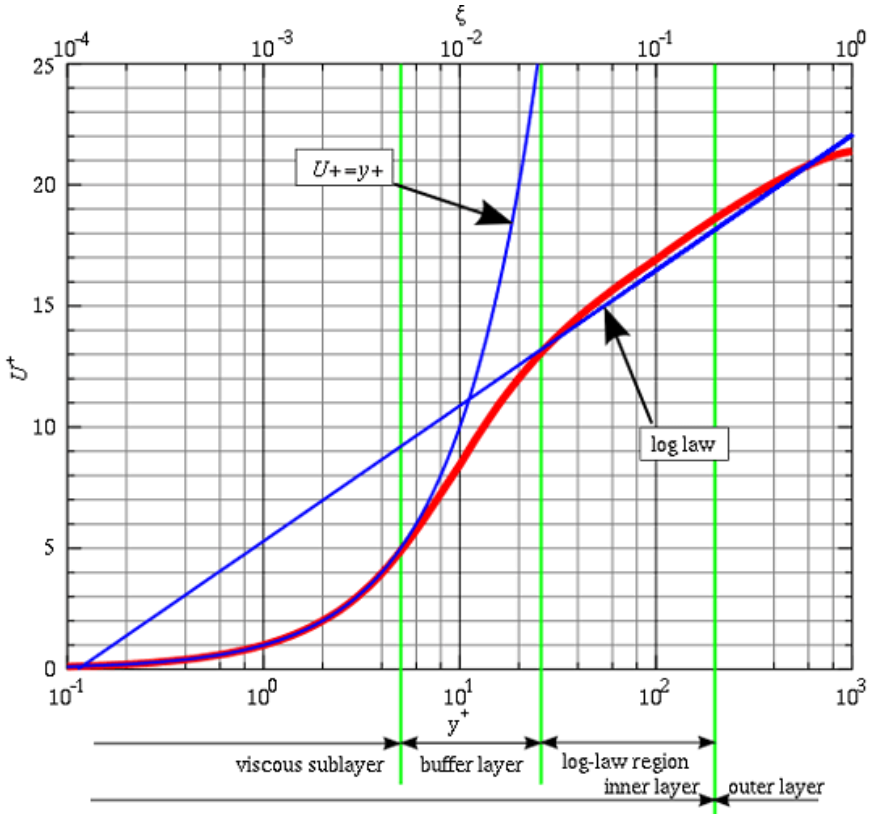

Figure 11. The Law of the Wall [14]

In the figure above, the "Law of the Wall" consists of 4 distinct regions: the viscous sublayer, the buffer layer, the inner layer, and the outer layer. Each region within the boundary layer has its own distinct flow characteristics. The viscous sublayer, which has y^+value less than 5, is characterized by purely laminar flow and viscous shear stresses. The velocity profile in this region is linear. The buffer layer, which has a y^+ between 5 and 30, is the transition layer between the laminar and turbulent regions. Viscous and turbulent stresses are of similar magnitude in this region and the velocity profile is not very well defined [14]. The log-law layer, which has a y^+ greater than 30, is characterized by turbulent flow and stresses. The velocity profile in this region varies very slowly with a logarithmic function along the distance y [14].

The equation for y^+ is defined in equation 3, where u_τ is the friction velocity,

$$y^+ = \frac{yu_\tau}{\upsilon} \qquad (3)$$

y is the boundary layer height, and υ is the kinematic viscosity of the fluid. The friction velocity can be approximated by equation 4 below,

$$u_\tau = \sqrt{\frac{\tau_{wall}}{\rho}} \qquad (4)$$

where τ_{wall} is the wall shear stress and it can be computed from equation 5.

$$\tau_{wall} = \frac{1}{2} C_f \rho U_\infty \qquad (5)$$

In equation 5 above, C_f represents the skin friction coefficient, which is estimated by equation 6. The equation below is for fully turbulent flow, but the relation will change for laminar flow.

$$C_f = \frac{0.026}{Re_x^{1/7}} \qquad (6)$$

Using the equations above, the various parameters in equations 4 through 6 can be calculated and substituted into a rearranged form of equation 3 that solves for y. This will result in the desired first cell height for the boundary layer.

Using this information, two approaches can be used to fully resolve the boundary layer near the wall. The first method involves resolving the boundary layer all the way down to the viscous sublayer, which is known as *near wall meshing*. This method requires an abundance of cells to be used due to how fine the mesh needs to be near the wall. Although you would accurately resolve the boundary layer, this may not be practical in most situations due to the computational resources needed and time. This method is best suited for when you are interested in the forces acting on the wall, like in blade optimization of turbomachinery [14]. The second method involves using wall functions, which can help model the near wall region without being computationally expensive. A further discussion of wall functions will come in the "Model Selection and Description" section.

Once a baseline mesh is developed, various metrics need to be assessed to judge whether this is a high-quality mesh. Two metrics that are often used are skewness and orthogonal quality. The skewness metric measures how close to ideal an element is, for example, how close a triangle element is to an equilateral triangle. A skewness value equal to 0 means a perfect element, while a skewness value equal to 1 means a degenerate element. It is recommended that the skewness be kept below 0.7 in general and below 0.85 for complex geometries. The orthogonal quality describes the quality of a volume mesh. It measures the angles between the cell faces and edges. Closer to 90-degree angles represents better alignment and improves solution accuracy. It it's recommended the orthogonal quality be kept above 0.1 whenever possible. Low quality elements will result in convergence issues, while high quality elements ensure a smoother simulation convergence.

Once the quality of the mesh is determined to be reasonable, a mesh sensitivity study can be conducted to ensure results are independent of the mesh. This involves altering the resolution of the mesh and observing how the results are affected by it. The optimal mesh density will balance both accuracy and computational time. A mesh that yields minimal changes in the results and low computational time is desired. This will ensure the most accurate results will be obtained to help make important design decisions.

For the NACA 0012 and NACA 64-006 models, a structured mesh was created using face meshing in FLUENT. Each quadrant of the fluid domain was meshed using quadrilateral elements. A mesh independence study for the NACA 0012 revealed a mesh density of 89,250 cells was the optimal mesh density. This mesh had an orthogonal quality of 0.97225 and a skewness of 0.063704. The NACA 64-006 model had a mesh density of 120,000 cells, an orthogonal quality of 0.96035, and a skewness of 0.081235. Neither model utilized inflation layers due to the mesh size around the airfoils being sufficient. The mesh for each model can be seen below in Figures 12 and 13.

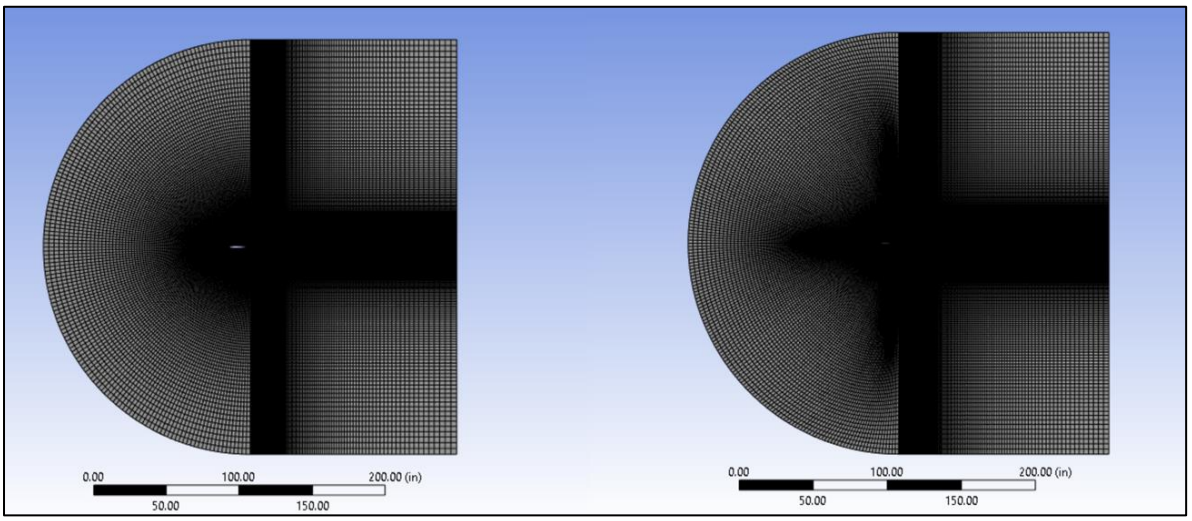

Figure 12. NACA 0012 (left) and NACA 64-006 (right) FLUENT mesh

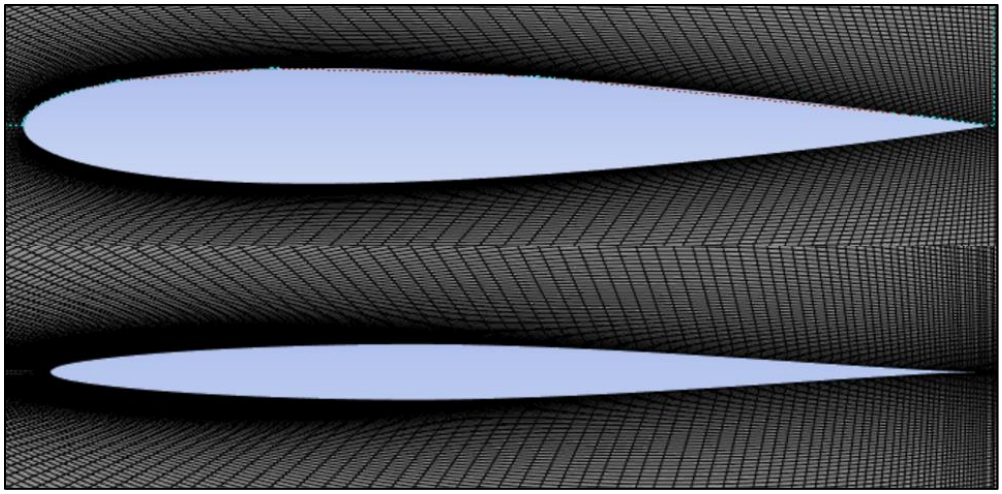

Figure 13. NACA 0012 (top) and NACA 64-006 (bottom) boundary layer mesh

For the flat plate delta wing and XQ-1A model, an unstructured mesh was generated due to the more complex designs involved. Due to the 512,000 cells count limit of Ansys Student, refining the mesh for more complex geometries can be tricky. Instead of investigating how the solution changes with mesh size, a baseline mesh was developed for both models that would capture the expected flow features and stay under the cell count limit. The results from each mesh were then validated with experimental and theoretical data to judge their appropriateness. The mesh for both the flat plate delta wing and XQ-1A models can be seen below in Figures 14 and 15.

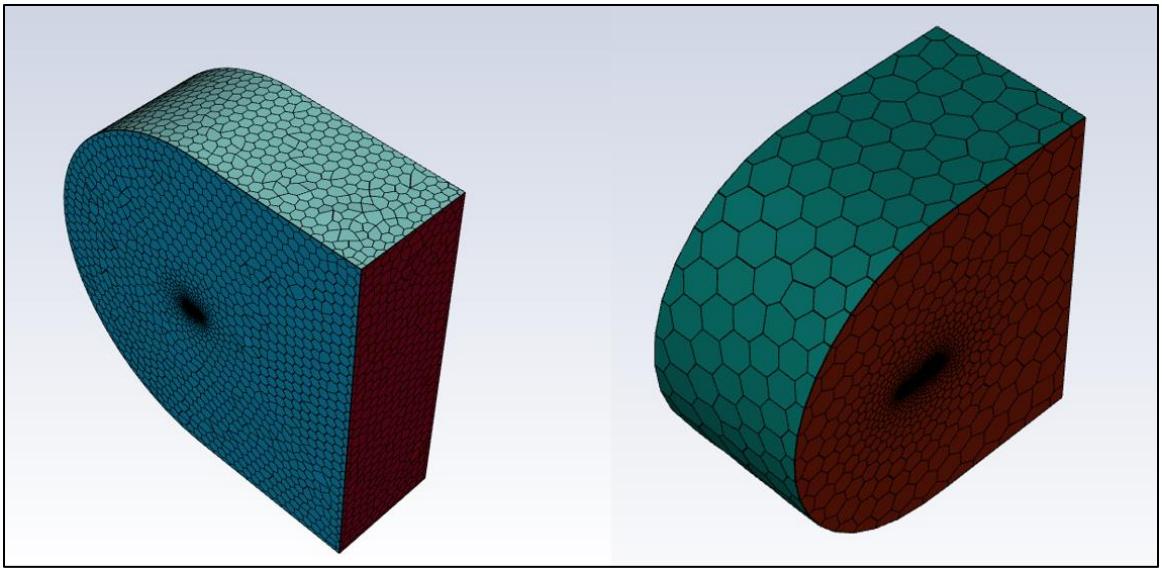

Figure 14. Flat plate delta wing (left) and XQ-1 (right) FLUENT mesh

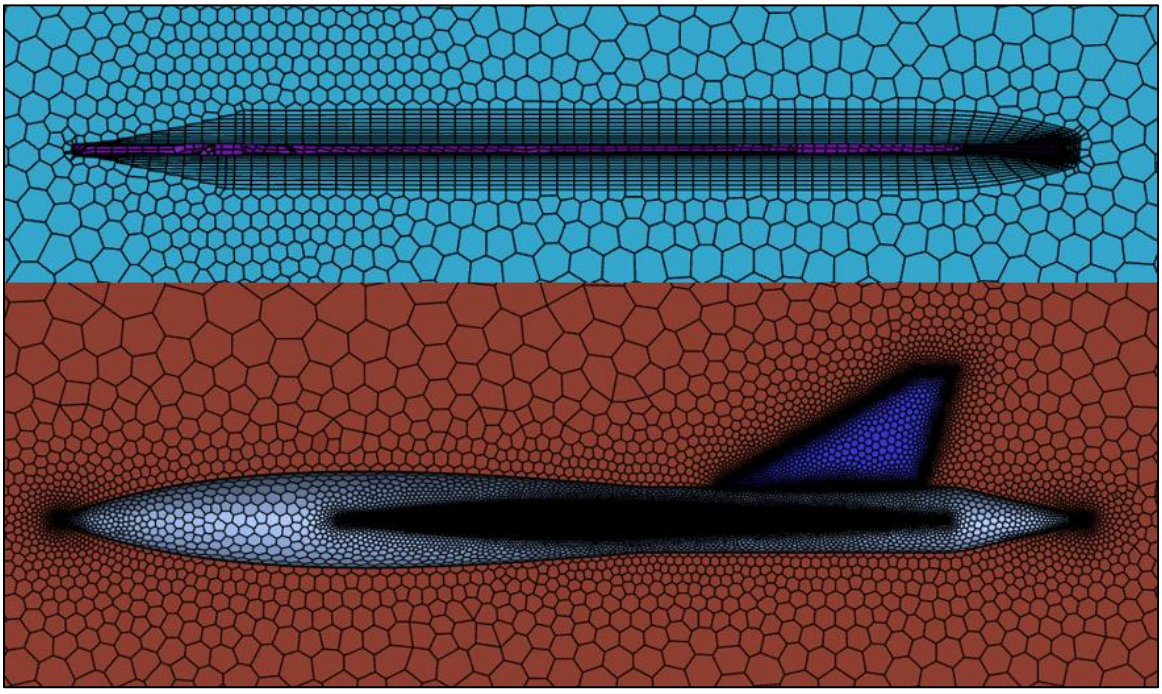

Figure 15. Flat plate delta wing (top) and XQ-1A (bottom) boundary layer mesh

For the flat plate delta, a mesh density of 313,690 cells, an orthogonal quality of 0.97018, and a skewness of 0.028588 was used. The boundary layer mesh consisted of 10 inflation layers with a first layer height of 0.0013 meters. For the XQ-1A, a mesh density of 506,231 cells, an orthogonal quality of 0.8957, and a skewness of 0.0884 was used. Due to the cell count limitation, no inflation layers were used to resolve the boundary layer. For both models, a y^+ value of around 30 was used for the mesh to ensure the boundary layer would be properly resolved using wall functions.

2.3.2 Model Selection and Description

To obtain numerically accurate results, selecting the correct model for CFD is important. Two key factors that impacted the model selection are the Reynolds number and the airfoil and wing geometry. The Reynolds number is a non-dimensional number that is used in fluid mechanics to classify the type of flow present in a fluid. It can be defined as the ratio of the inertial effects to the viscous effects present in a fluid. As seen in equation 7, the Reynolds number is dependent on the density, dynamic viscosity, and velocity of the fluid, as well as the characteristic length of the system.

$$Re = \frac{\rho V L}{\mu} \qquad (7)$$

For external flow problems, experiments involving flow over a flat plate have revealed after a certain length of flow, the laminar boundary layer transitions into a turbulent flow. This usually happens at the critical Reynolds number, which is defined as $Re_{x,cr} =$

5×10^5. Since simulations are being run at a Reynolds number of 5×10^5 and 3×10^6, we expect turbulent flow to be present.

In addition, the airfoil and wing geometry played a role in determining the use of a turbulence model. At high angles of attack, we expect the flow over the NACA 0012 and NACA 64-006 airfoils to separate and become turbulent along the top surfaces. Likewise, for the delta wing at very high angles of attack, we expect the leading-edge vortices to breakdown and decay into turbulence. For these reasons, along with the Reynolds number, the use of a turbulence model was deemed fitting.

Ansys FLUENT offers a wide array of turbulence models to select from. Two methods that are available to model turbulence are the Reynolds Average Navier Stokes (RANS) model and the Large Eddy Simulation (LES) model. The RANS model uses an averaged form of the Navier Stokes equations, which includes additional terms to solve for the Reynolds Stress terms [15]. By solving for the averaged quantities of the flow, the whole range of the scales of turbulence can be modeled [11]. The RANS model is one of the most widely used models in industry due to its low computational cost and ability to handle complex geometries. The LES model utilizes a "filtered" form of the Navier Stokes equation to resolve large eddies in a time dependent solution [11]. Filtering is the mathematical manipulation of the Navier Stokes equation to remove the smaller eddies that are smaller than the filter, which is the mesh size in this case [11]. The concept behind LES is that by modeling less of the turbulence (and resolving more), the error introduced by turbulence modeling can be reduced [11]. LES tends to be more accurate than RANS modeling, but this comes at the cost of being more computationally

expensive and requiring greater computational resources. Due to these reasons, a RANS model was selected for this research.

Ansys FLUENT offers various RANS models, such as the Spalart-Allmaras, $k-\varepsilon$ and its variants, $k-\omega$ and its variants, and Reynolds Stress Model (RSM). These RANS models are based on the RANS equation, which can be seen below in its tensor form [15].

$$\frac{\partial(\rho U_i)}{\partial t}+\frac{\partial(\rho U_i U_j)}{\partial x_j}=-\frac{\partial P}{\partial x_i}+\frac{\partial}{\partial x_j}[\mu\left(\frac{\partial U_i}{\partial x_j}+\frac{\partial U_j}{\partial x_i}\right)-\rho\overline{u_i{}'u_j{}'}] \quad (8)$$

In the RANS equation, U is the mean flow velocity, u' is the velocity fluctuations due to turbulence, μ is the dynamic viscosity of the fluid, and $\overline{u'J'}$ is the Reynolds Stress term. To solve the RANS equation, the Reynolds stress term needs to be expressed in terms of mean flow quantities [15]. The solution for the Reynolds stress term is known as the Eddy viscosity hypothesis or Boussinesq hypothesis, which can be seen below in equation 9 [15].

$$-\rho\overline{u'J'}=\mu_t(\frac{\partial U_i}{\partial x_j}+\frac{\partial U_j}{\partial x_i}-\frac{2}{3}\frac{\partial U_k}{\partial x_k}\delta_{ij})-\frac{2}{3}\rho k\delta_{ij} \quad (9)$$

In equation 9, μ_t is the turbulent or eddy viscosity and δ_{ij} is the Kronecker Delta. This equation reveals that to solve the RANS equation, the turbulent viscosity needs to be solved for first [15]. Thus, the difference between these turbulence models is how they solve for the eddy viscosity.

Each of these models has its own benefits and drawbacks. For this research the Realizable $k-\varepsilon$ model, a two-equation turbulence model, was selected. This means it solves two additional transport equations in addition to the conservation equations. These two transport equations solve for the turbulent kinetic energy (k) and the turbulent energy dissipation rate (ε) [15]. Turbulent kinetic energy determines how much energy is in the turbulence and turbulent energy dissipation rate determines the rate at which the turbulent kinetic energy is dissipated [15]. The partial differential equations (PDE) for turbulent kinetic energy and turbulent energy dissipation rate can be seen below in equations 10 and 11 respectively.

$$\frac{\partial(\rho k)}{\partial t}+\frac{\partial(\rho U_i k)}{\partial x_i}=\frac{\partial}{\partial x_j}\left[\left(\mu+\frac{\mu_t}{\sigma_k}\right)\frac{\partial k}{\partial x_j}\right]+P_k+P_b-\rho\epsilon+S_k \tag{10}$$

$$\frac{\partial(\rho \epsilon)}{\partial t}+\frac{\partial(\rho U_i \epsilon)}{\partial x_i}=\frac{\partial}{\partial x_j}\left[\left(\mu+\frac{\mu_t}{\sigma_k}\right)\frac{\partial \epsilon}{\partial x_j}\right]+\rho C_1 S_\epsilon-C_2\rho\frac{\epsilon^2}{k+\sqrt{\upsilon\epsilon}}+C_1\frac{\epsilon}{k}C_3P_b+S_\epsilon \tag{11}$$

In equation 10, P_k is the production of turbulent kinetic energy (TKE) due to mean velocity shear, P_b is the production of TKE due to buoyancy, S_k is the user defined source, and σ_k is the turbulent Prandtl number for k. In equation 11, C_1, C_2, σ_k, and σ_ϵ are known constants. The values of these constants are $C_1=1.44$, $C_2=1.92$, $\sigma_k=1$, and $\sigma_\epsilon=1.3$ [15]. It has been found that the Realizable $k-\varepsilon$ model provides the best performance of all the $k-\varepsilon$ variants at predicting separated flow and complex secondary flow features [11]. Furthermore, it has low computational cost and robust convergence.

Due to these reasons, it was determined that this model would be the best option for modeling flow over a delta wing.

To properly model the boundary layer flow across the delta wing, the Realizable $k-\varepsilon$ model can utilize wall functions. Wall functions are empirical equations that help satisfy the physics of the flow in the near wall region. To properly use wall functions, the first cell center needs to be placed in the log-law layer to ensure the accuracy of the results [16]. Wall functions are used to bridge the inner region between the wall and fully developed turbulent region. Furthermore, they provide near-wall boundary conditions for the momentum and turbulence transport equations, rather than specifying those conditions at the wall itself [16]. The use of wall functions vastly decreases the mesh size needed to fully resolve the boundary layer, which decreases the computational cost. This approach is very beneficial for those with limited computational resources and provides robust and accurate results. Ansys FLUENT offers various wall functions for its turbulence models, such as standard wall functions, scalable wall functions, non-equilibrium wall functions, enhanced wall treatment, user defined wall functions, and LES near wall treatment. Scalable wall function was selected due to it ensuring that the CFD solvers y^+ was greater than 11.225 regardless of boundary layer mesh size. This wall function ensures that the turbulent portion of the boundary layer (log-law region) gets resolved.

2.3.3 Domain Boundary Conditions

Boundary conditions are critical for CFD simulations because they define how a system interacts with its surroundings. Determining the appropriate boundary conditions for simulations are important to obtain physically accurate results. In FLUENT, boundary conditions are utilized by the governing equations and additional equations important for the flow physics being simulated. These equations are solved for various unknown parameters, such as velocity, pressure, and temperature. Depending on the type of problem, various boundary conditions can be assigned in FLUENT. For the NACA 0012 and NACA 64-006 models, three boundary conditions were used: velocity inlet, wall, and pressure outlet. These three boundary conditions can be seen below in Figure 16.

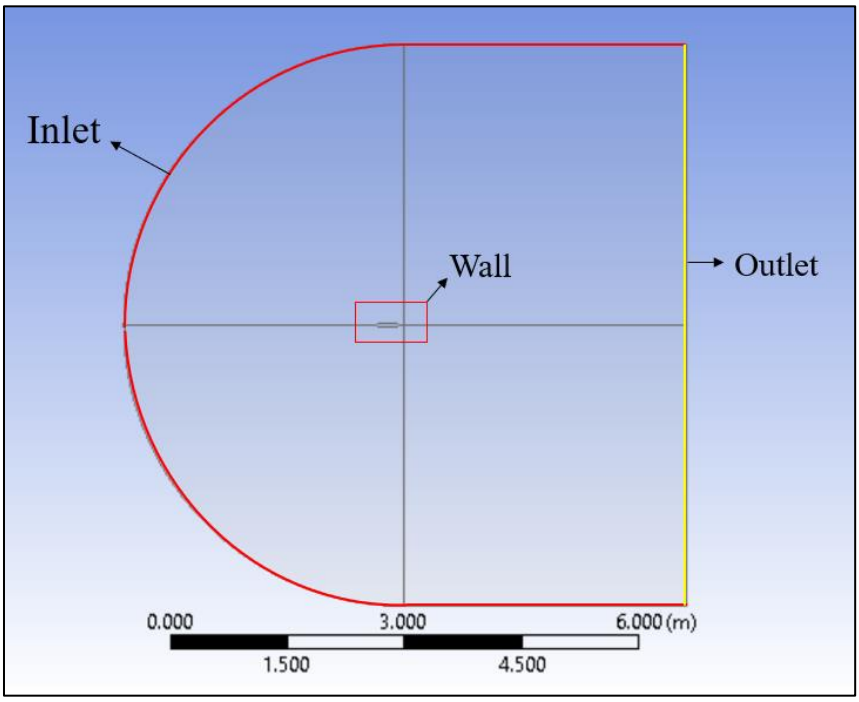

Figure 16. Boundary conditions for the NACA 0012 an NACA 64-006 models

The velocity inlet in red consists of the arc, top edge, and bottom edge. At the velocity inlet, free stream air flow enters the system at a velocity of 20.283 m/s for a $Re = 5 \times 10^5$ and 121.7 m/s for a $Re = 3 \times 10^6$. Using the velocity "components" method, the x and y components of the velocity at a particular angle of attack can be set. Likewise, the pressure outlet consists of the back two yellow edges of the fluid domain. The pressure outlet is where the air flow exits, and the gauge pressure can be set at this location. Since the operating conditions are standard day conditions, the gauge pressure was set to 0 Pa. The airfoils in the models were designated as walls, where the "no slip" condition applies. The no slip condition states that at the fluid-wall interface, the velocity of the fluid is equivalent to the velocity of the wall. This means any fluid that is "stuck" to the wall will have zero velocity.

For the flat plate delta and XQ-1A models similar boundary conditions were applied. These boundary conditions can be seen below in Figure 17.

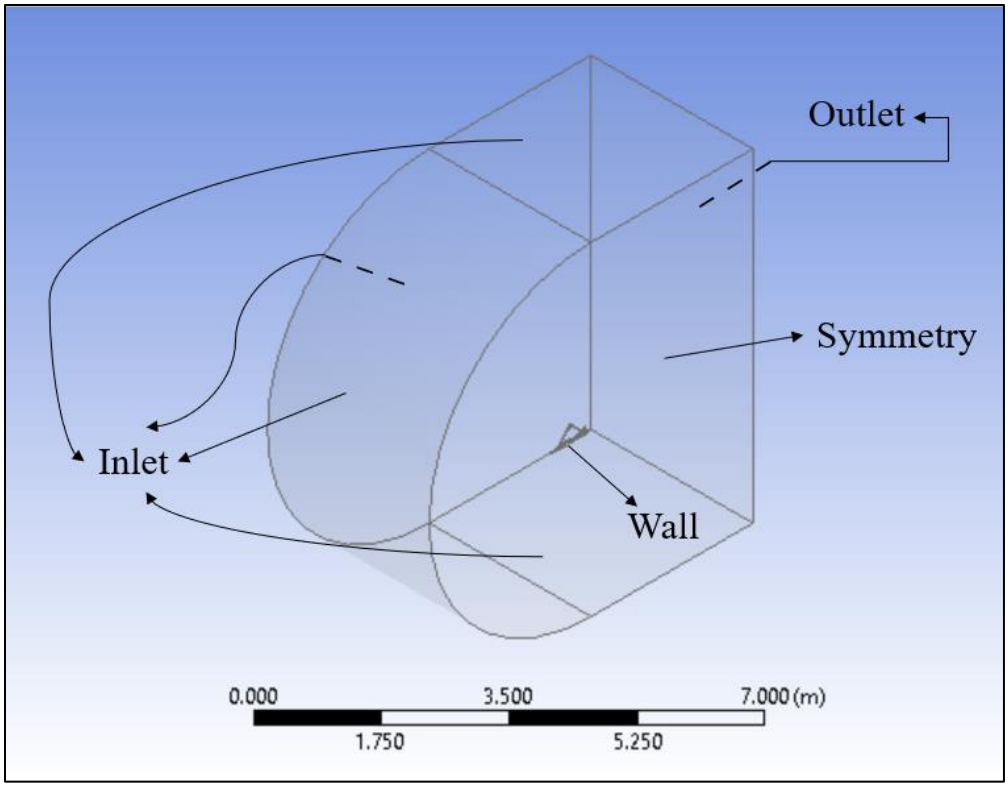

Figure 17. Boundary conditions for the flat plate delta wing and XQ-1A models

The velocity inlet consists of the arc, left face, top face, and bottom face of the fluid domain. For the velocity inlet, the velocity was set using the "components" method and was specified as 20.283 m/s. The pressure outlet is designated at the back face of the fluid domain and the gauge pressure was specified as 0 Pa. The wall condition was applied to the delta wing and XQ-1A, which were specified as a "no-slip" wall. In addition to these boundary conditions, a symmetry boundary condition was specified at the right face for both models. The symmetry boundary condition can be used when the geometry of interest and expected fluid flow have mirror symmetry. At the symmetry boundary

condition, FLUENT assumes a zero flux of all quantities across a symmetry boundary [11]. Since there is no convective flux across a symmetry plane, the normal velocity component at the symmetry plane is thus zero [11]. In viscous flow problems, this symmetry plane can be treated as a “slip wall”, where the fluid is not fixed to the wall [11]. The use of this boundary condition helps reduce the overall size of the computational domain to a symmetric subsection of the fluid domain. This will result in the computational cost and time needed for the simulation to be reduced.

Chapter 3. Results and Discussion

This chapter discusses the results of the various CFD models that were created. The resultant flow field visualizations are discussed first. This includes pressure, velocity and streamline contours. Finally, the model validation and verification process are discussed. This process involved comparing the CFD results with both experimental and theoretical data. The theoretical data was generated using Polhamus's leading edge suction analogy. The following plots for each model's results will be provided: lift curve, drag polar, and aerodynamic efficiency.

3.1 Resultant Flow Field Visualization

Ansys FLUENT offers various means to post process results of CFD simulations. These include various types of pressure and velocity contours, and streamlines. These contours are meant to give engineers valuable information on various quantities that impact the aerodynamics of an aircraft. Utilizing this information, aircraft performance can be optimized to meet designated design requirements. In the proceeding sections, pressure contours, velocity contours, and streamlines for each CFD model will be discussed.

3.1.1 Pressure Contours

Pressure contours are an important flow visualization tool that show the pressure distribution along an aircraft's geometry due to the fluid-body interactions experienced during flight. Pressure is defined as the normal force per unit area exerted on a surface due to the time rate of change of momentum of the gas molecules impacting on the surface. Pressure is defined as a point property, which means that it can vary by location in the flow field. The aerodynamic forces acting on a body moving through the air are due to two basic sources, the pressure and shear stress distributions exerted on the body surface. The pressure distribution acting along the body is predominantly responsible for generating the lift of any aerodynamic body, while the shear stress distribution contributes marginally to the lift. On the other hand, drag is generated by both the pressure and shear stress distributions. By characterizing the pressure distribution along an aircraft's geometry, a better understanding of the aircraft's performance can be obtained.

For the NACA 0012 model, the pressure contours for various angles of attack can be seen below in Figure 18.

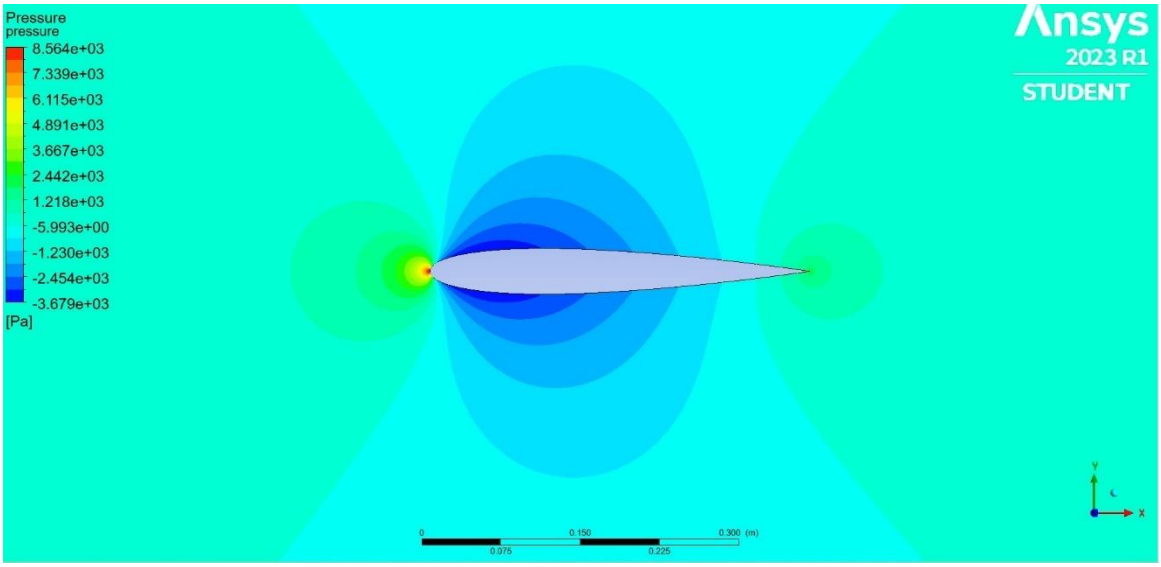

a) NACA 0012 airfoil, $\alpha = 0°$

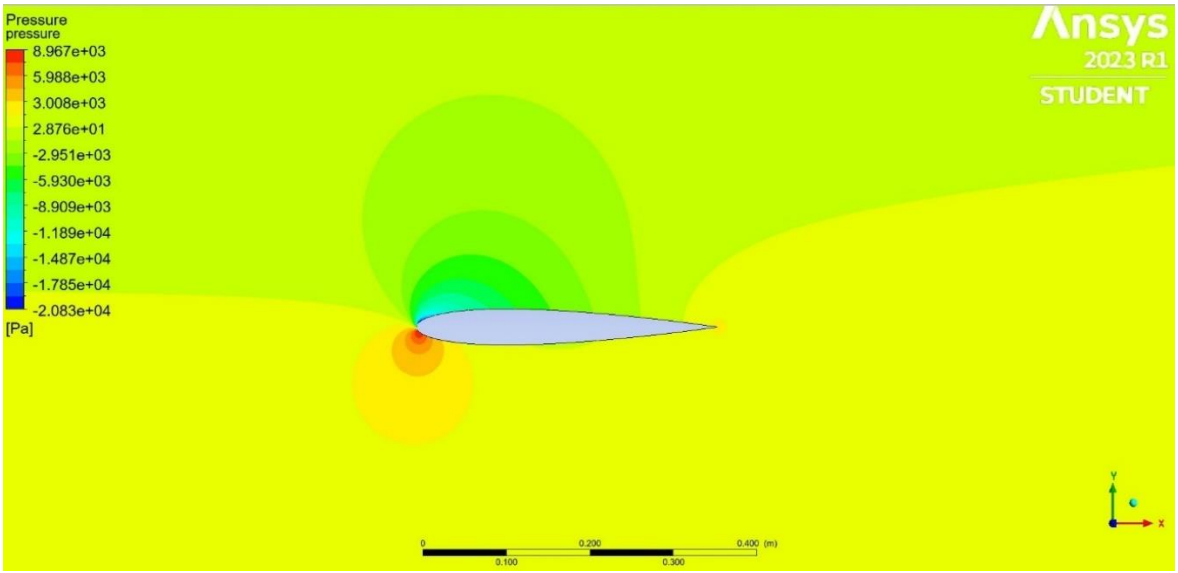

b) NACA 0012 airfoil, $\alpha = 6°$

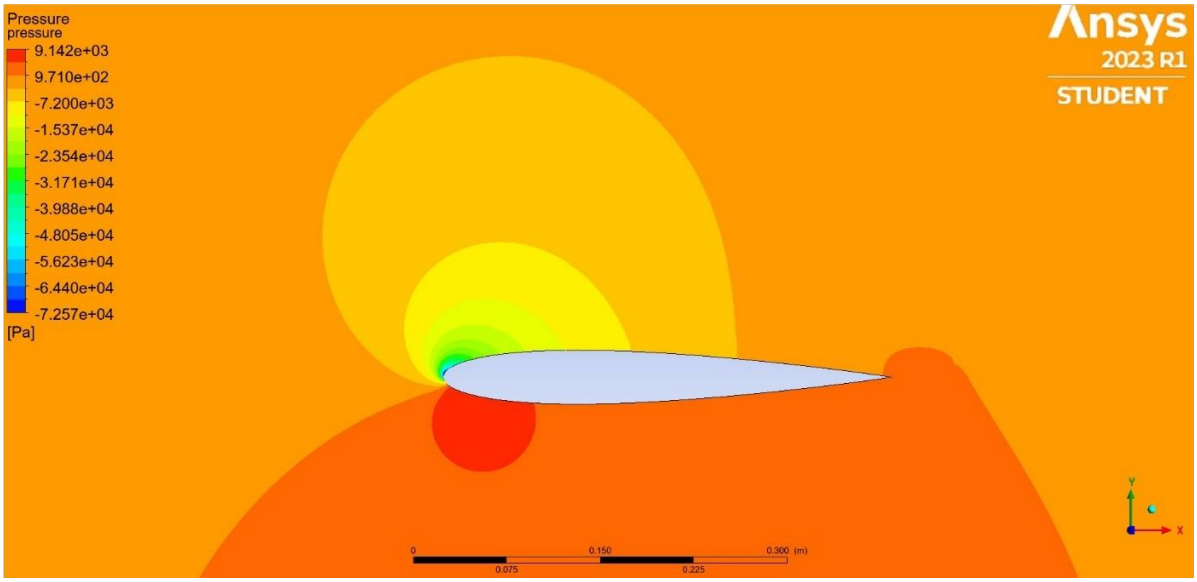

c) NACA 0012 airfoil, $\alpha = 14°$

Figure 18. Pressure distribution over the NACA 0012 airfoil at a Re = 3M

At $\alpha = 0$ degrees, there is a rapid drop in pressure in the proximity of the airfoil (indicated by blue regions) in comparison to the upstream and downstream pressure (indicated by green regions). This is due to the airfoil impeding the airflow, which is altering the local velocity of the flow from the freestream velocity. At the front of the airfoil, a stagnation point develops where the local velocity of the flow is zero. This is due impart to the very large static pressure generated at the front of the airfoil (indicated by small red region). The airflow must rapidly increase its velocity to get around the airfoil before it returns to the freestream velocity. For this to happen, the pressure along the airfoil must drop below the freestream pressure initially and gradually increase back to freestream conditions. This can be seen above as the blue regions near the airfoil

slowly transition from blue to green, indicating an increase in the local pressure back to the freestream conditions. In addition, the pressure distribution along the airfoil is symmetric due to the NACA 0012 being symmetric.

As the angle of attack increases, the pressure distribution along the NACA 0012 airfoil begins to change. This alteration in the pressure distribution is expected due to the increase in lift that occurs with an increase in angle of attack. For lift to be generated, there must be a net pressure difference between the top and bottom surfaces in the vertical direction. In addition, the stagnation point at the front of the airfoil begins to move further downstream. At $\alpha = 6$ degrees and $\alpha = 14$ degrees, the bottom surface of the airfoil experiences an increase in local pressure above the freestream pressure (indicated by the yellow and orange regions respectively). On the other hand, the top surface experiences a drop in local pressure below the freestream pressure. As the angle of attack increases, the local pressure near the trailing edge begins to become greater than the local pressure near the leading edge. This increase in pressure near the trailing edge causes a mild adverse pressure gradient, which causes the airflow to begin to separate from the airfoil at $\alpha = 14$ degrees.

The NACA 64-006 airfoil exhibited different pressure characteristics in its flow field compared to the NACA 0012. The pressure contours for the NACA 64-006 airfoil can be seen below in Figure 19.

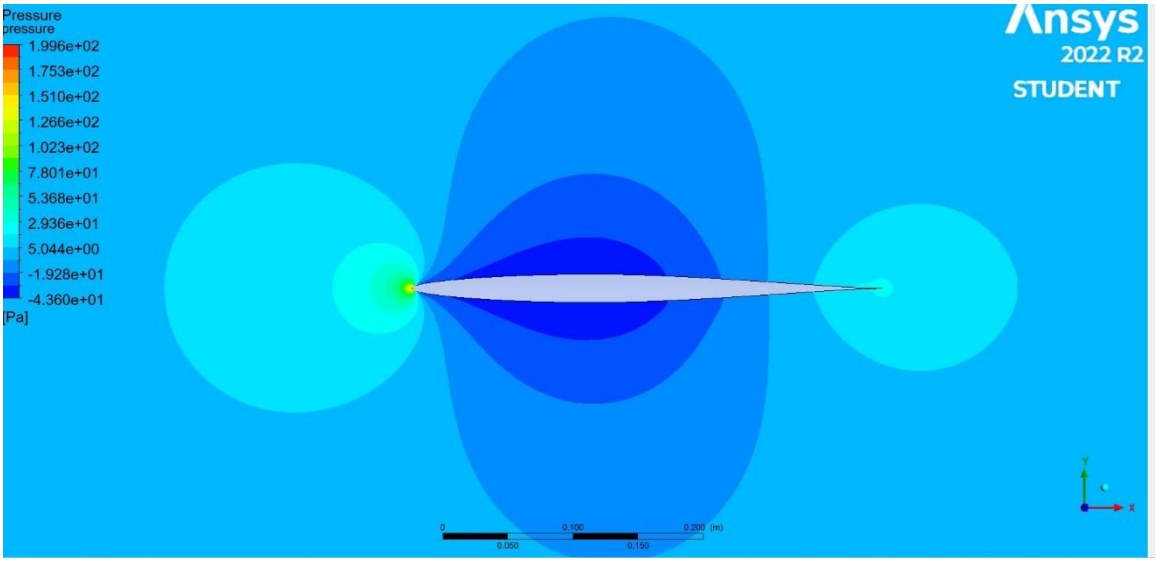

a) NACA 64-006 airfoil, $\alpha = 0°$

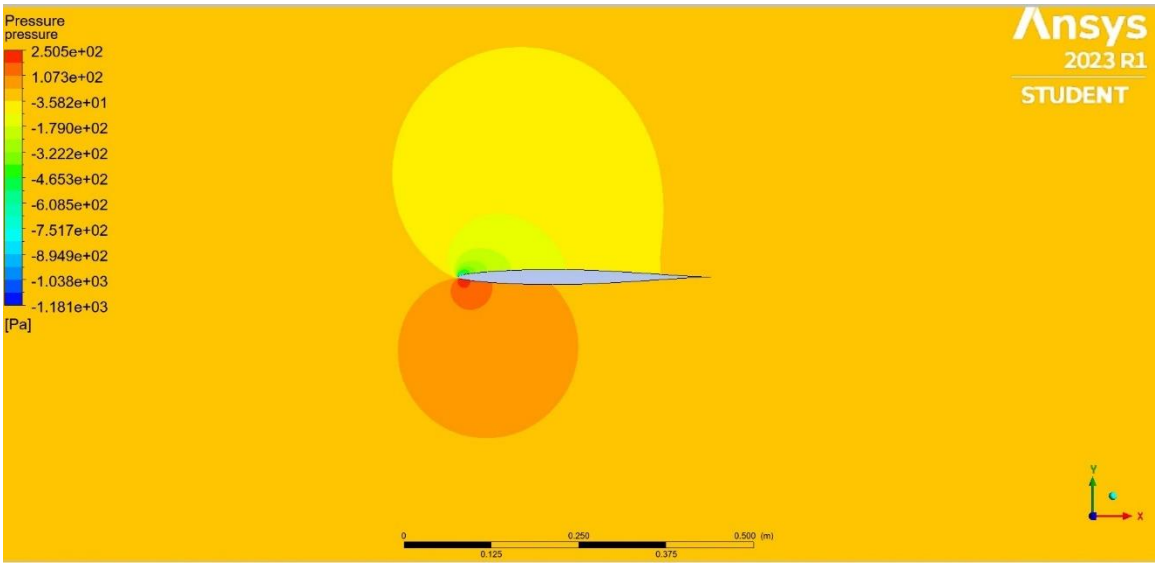

b) NACA 64-006 airfoil, $\alpha = 8°$

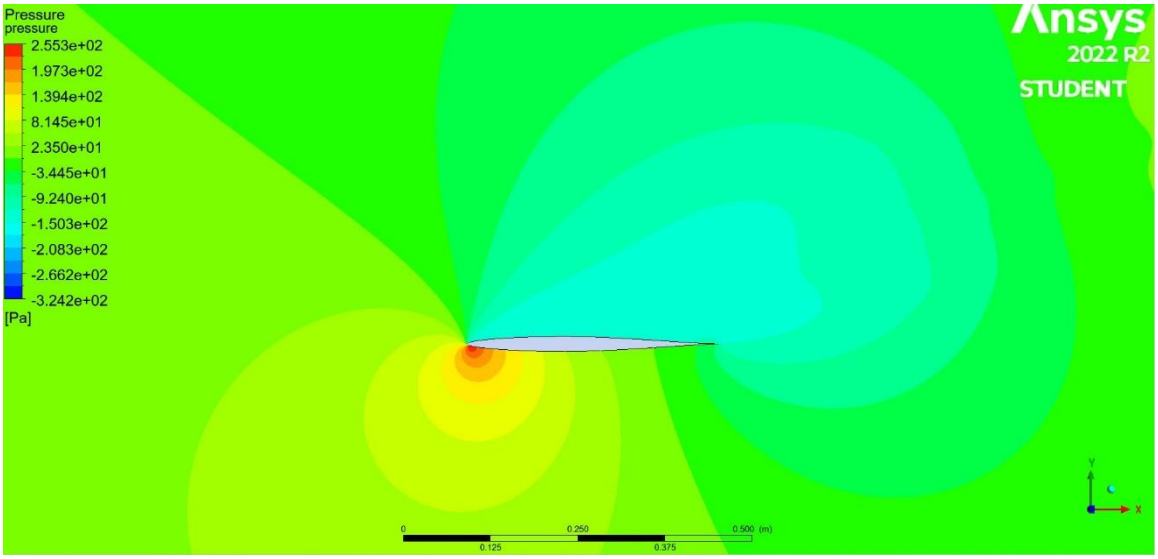

c) NACA 64-006 airfoil, $\alpha = 20°$

Figure 19. Pressure distribution over the NACA 64-006 airfoil at a Re = 500K

At $\alpha = 0$ degrees, the pressure drops below the freestream pressure in the proximity of the airfoil. As stated before, the velocity of the airflow will be greater than the freestream velocity in these areas of low pressure. These areas of low pressure gradually transition back to the freestream pressure near the trailing edge. This results in the velocity of the airflow returning to the freestream velocity. At the very front of the airfoil, a stagnation point can be observed where the velocity of the flow is zero. As the angle of attack increases, this stagnation point moves further downstream and a clear difference in pressure between the top and bottom surfaces is observed.

At $\alpha = 8$ degrees, the pressure near the trailing edge (indicated in orange) is higher than the pressure at the leading edge (indicated in yellow and green), which shows

an adverse pressure gradient developing. As this adverse pressure gradient develops, it will ultimately result in flow separation. At $\alpha = 20$ degrees, there is a low-pressure region along the top surface of the airfoil and in the wake behind it. This low-pressure region is usually associated with flow separation, which in this case is completely detached from the airfoil at $\alpha = 20$ degrees. If the flow were attached to the airfoil still, the pressure that would exist along the airfoil would be much greater than what is observed.

For the flat plate delta wing model, the pressure distribution obtained was much different from the airfoils due to the delta wing's inherently non-linear aerodynamics. The pressure coefficient contours for the flat plate delta wing can be seen below in Figure 20.

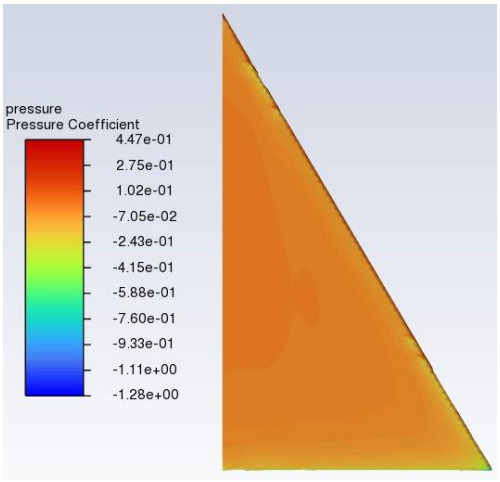

a) Top surface, $\alpha = 0°$

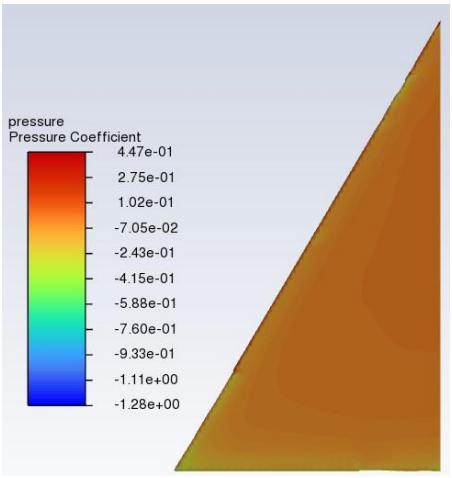

b) Bottom surface, $\alpha = 0°$

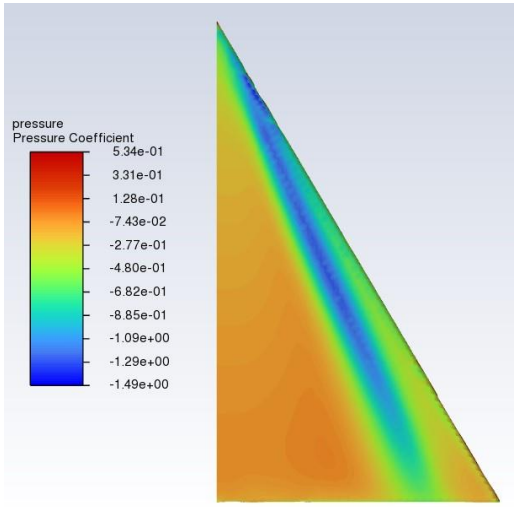

c) Top surface, $\alpha = 10°$

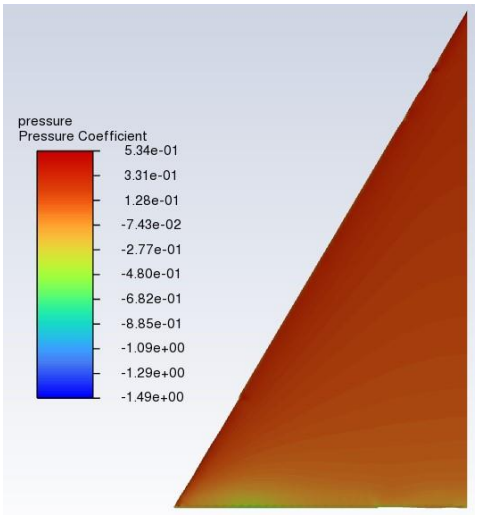

d) Bottom surface, $\alpha = 10°$

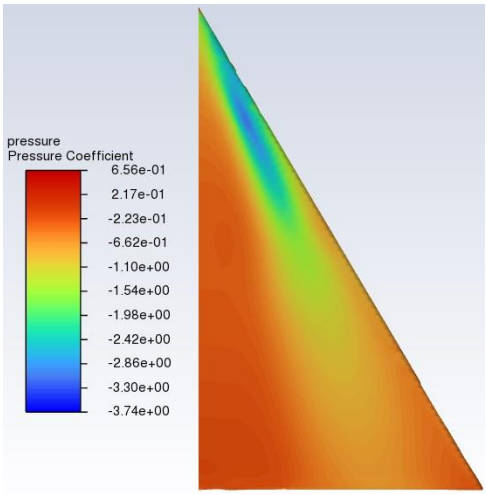

e) Top surface, $\alpha = 20°$

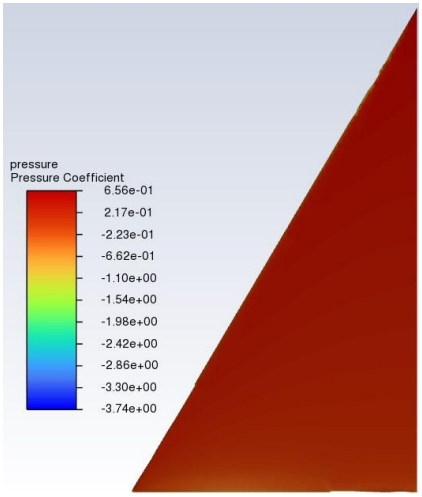

f) Bottom surface, $\alpha = 20°$

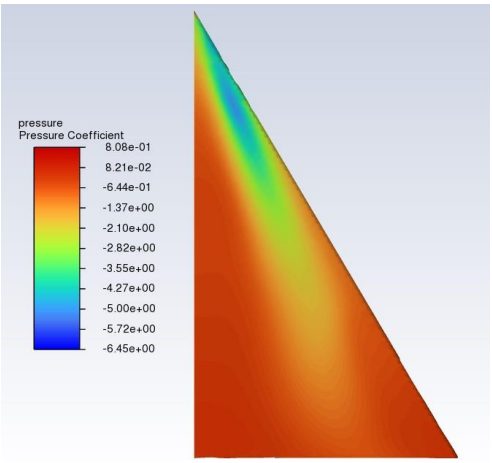

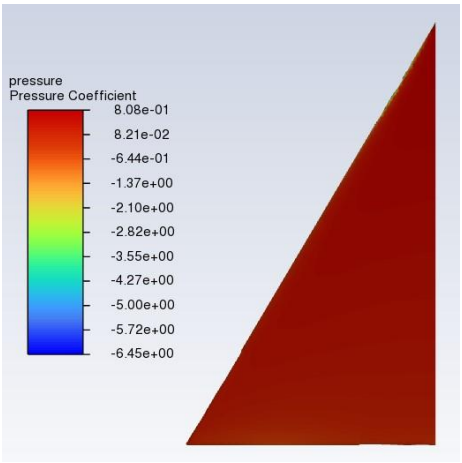

g) Top surface, $\alpha = 30°$ h) Bottom surface, $\alpha = 0°$

Figure 20. Pressure distribution over a flat plate delta wing at a Re = 500K

At $\alpha = 0$ degrees, the pressure coefficient distribution on the top and bottom surfaces of the wing are uniform in the spanwise direction. However, this changes as the angle of attack increases. At $\alpha = 10$ degrees, the pressure on the bottom surface has increased but remains uniform in the spanwise direction (indicated by the dark orange region). This increase in pressure on the bottom side makes sense due to the lift being generated by a pressure difference between the top and bottom surfaces of the wing. However, along the top surface of the wing, the local pressure inboard of the leading edge drops significantly below the freestream pressure (indicated by blue and green regions). This drop in the local pressure in these regions is characteristic of the leading-edge vortex. The presence of these vortices contributes to additional lift being generated by creating a strong

"suction" effect near the leading edges of the wing. This is the main reason why the delta wing typically has a higher stall angle compared to conventional wing planforms.

As the angle of attack increases beyond 10 degrees, the pressure distribution on the bottom surface remains constant in the spanwise direction but greater in magnitude (indicated by the dark red regions). However, along the top surface of the wing, the local pressure inboard of the leading edge begins to increase. This indicates the presence of vortex breakdown, which results in the decay of these vortices. At $\alpha = 20$ degrees and $\alpha = 30$ degrees, the area of the wing directly inboard of the leading edge has far less surface area covered by local pressure below the freestream pressure. This means only a portion of the vortex still exists along the wing (located in the blue regions).

For the XQ-1A full aircraft model, simulation results showed some similarities and differences with the flat plate delta wing model. The pressure coefficient contours can be seen below in Figure 21.

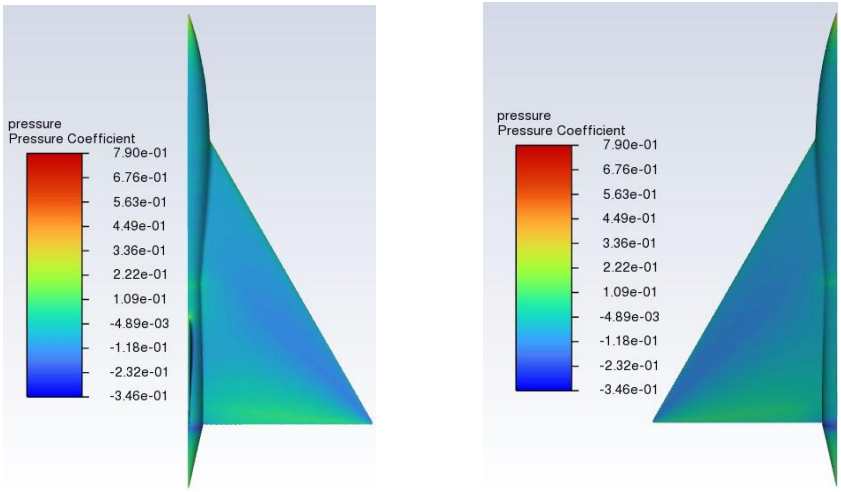

a) Top surface, $\alpha = 0°$

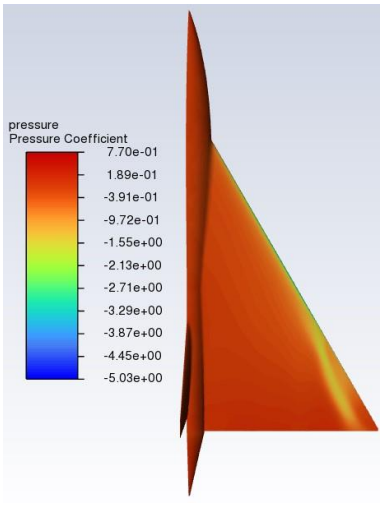

b) Bottom surface, $\alpha = 0°$

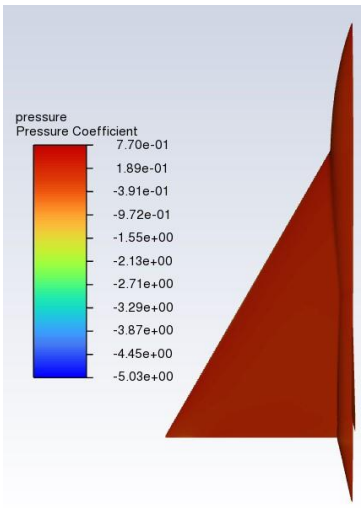

c) Top surface, $\alpha = 10°$

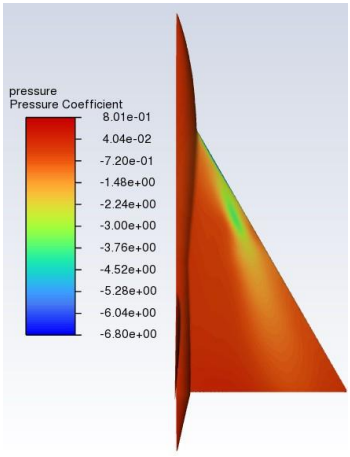

d) Bottom surface, $\alpha = 10°$

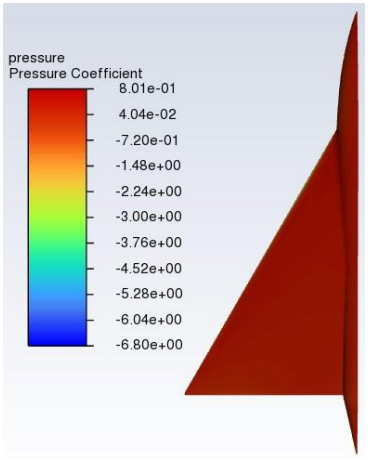

e) Top surface, $\alpha = 20°$

f) Bottom surface, $\alpha = 20°$

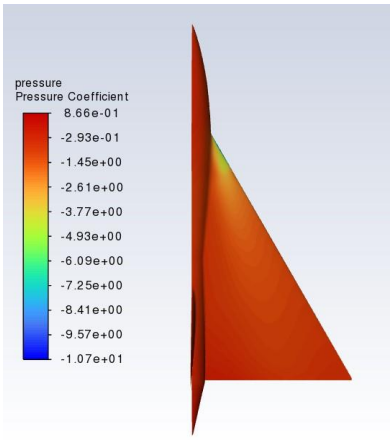

g) Top surface, $\alpha = 30°$

Figure 21. Pressure distribution over the XQ-1A at a Re = 500K

At $\alpha = 0$ degrees, the pressure distribution in the spanwise direction on the top and bottom surface is not uniform like the flat plate delta wing. This is due to the wing-body interaction of the XQ-1A's fuselage with the delta wing. The flow over the fuselage will alter the flow over the wing, and vice versa. This alteration in the flow field would alter the pressure distribution observed along the delta wing. Portions of the fuselage and wing have regions of low local pressure (indicated in blue) and regions of higher local pressure (indicated in green). These areas of low local pressure are where the local velocity will be the highest, while the areas of higher pressure will have a lower local velocity.

As the angle of attack increases, the leading-edge vortex begins to form inboard of the leading edge. At $\alpha = 10$ degrees, a low-pressure region develops on the top surface inboard of the leading edge, indicating the formation of the leading-edge vortex. A noticeable difference between the XQ-1A and flat plate delta wing model is the local

low-pressure region covering the top surface is much smaller for the XQ-1A than the flat plate delta wing. On the bottom surface of the wing, the pressure distribution increases in magnitude and is uniform in the spanwise direction. This trend continues as the angle of attack increases. At $\alpha = 20$ degrees, the leading-edge vortex is already fully formed, but exhibits signs of vortex breakdown due to an increase in local pressure in the region where the vortices form (indicated by the light and darker yellow regions). As the angle of attack increases to 30 degrees, the low-pressure regions inboard of the leading-edge cover a minimal area of the wing. This means the vortex breakdown continued and resulted in the leading-edge vortex decaying even further.

3.1.2 Velocity Contours

Velocity contours are utilized to visualize the speed and direction of airflow around an aerodynamic body. These contours are important for designing both a safe and efficient aircraft. The velocity contours for the NACA 0012 airfoil can be seen below in Figure 22.

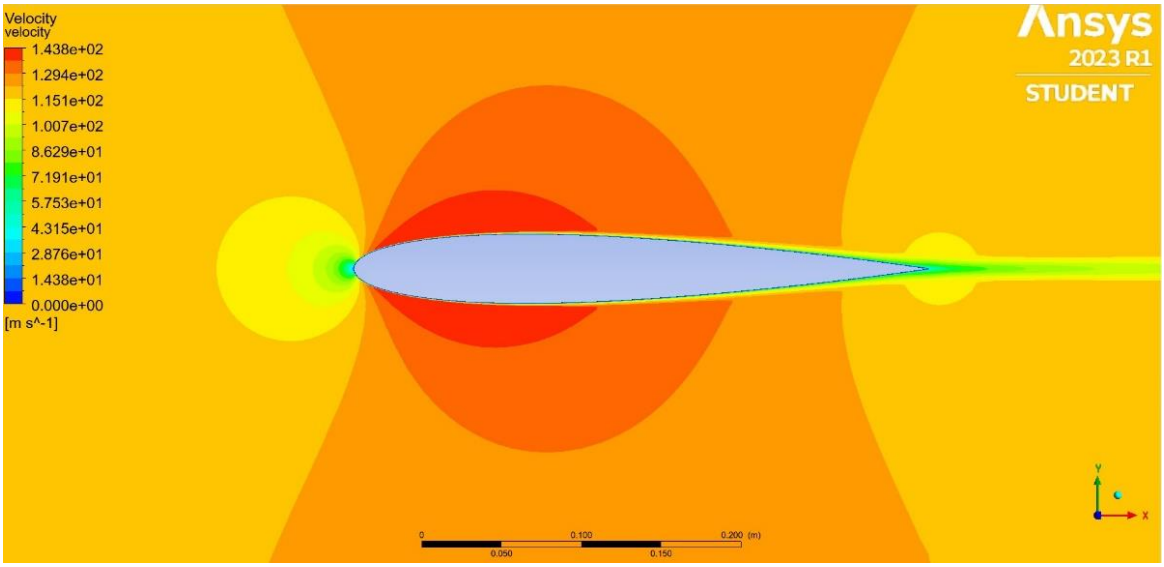

a) NACA 0012 airfoil, $\alpha = 0°$

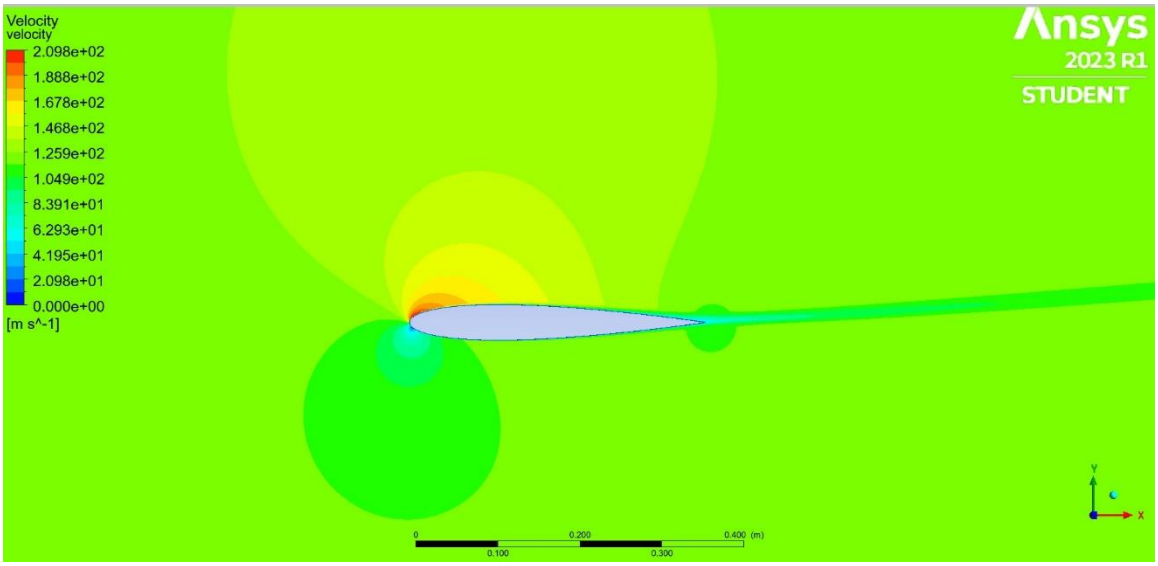

b) NACA 0012 airfoil, $\alpha = 6°$

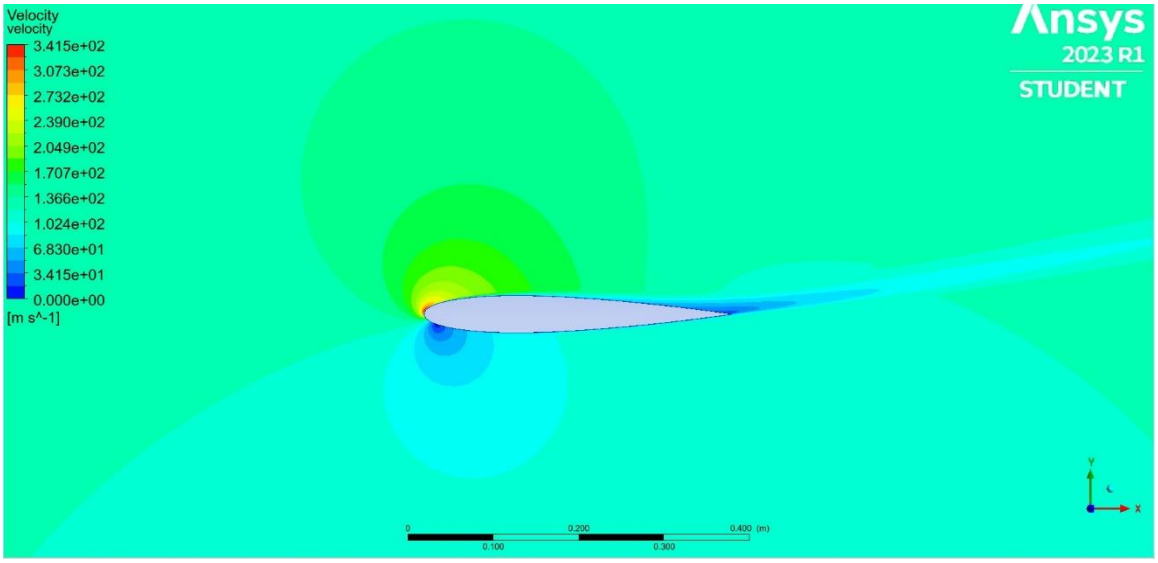

c) NACA 0012 airfoil, $\alpha = 14°$

Figure 22. NACA 0012 airfoil velocity flow field at various angles of attack

At $\alpha = 0$ degrees, the local velocity of the flow in the proximity of the top and bottom surfaces of the airfoil is greater than the freestream velocity further upstream and downstream of the airfoil (indicated by orange and red regions). However, at the front and rear of the airfoil, the local velocity of the flow is less than the freestream velocity (indicated by yellow and green regions). Due to the subsonic flow, disturbances in the airflow propagate throughout the entire flow field. This is seen above as certain regions away from the airfoil have either lower or higher local velocities compared to the freestream.

An interesting feature at the front of the airfoil is a point where the local velocity is zero (indicated by the blue region). This is known as the stagnation point. Two

stagnation points exist on an airfoil, which are at the leading and trailing edges. Looking at the boundary layer on the airfoil's surface, it's clear that it is fully laminar. The velocity at the surface is zero due to friction causing the air molecules to stick (no-slip condition). As you move further away from the airfoil surface, the velocity increases back to the freestream velocity at the edge of the boundary layer. This is due to the viscous effects in the boundary layer becoming less influential the further away the airflow is from the surface of the airfoil.

As the angle of attack increases, the local velocity of the airflow on the bottom surface decreases below the freestream velocity due to a rise in static pressure. However, on the top surface, there is a drop in static pressure, which results in regions of the airfoil having a higher local velocity. At $\alpha = 6$ degrees and $\alpha = 14$ degrees, the local velocity near the leading edge is much greater than the freestream velocity (indicated by red and orange regions). As the airflow moves towards the leading edge, the local velocity begins to drop. Furthermore, the stagnation point at the leading edge becomes more prominent and moves further downstream of the airfoil. This increase in prominence is because more airflow is being impeded by the airfoil's presence. At $\alpha = 14$ degrees, a region where the local velocity is near zero develops near the trailing edge. The presence of "dead air" in this region is characteristic of separated flow, which appears to start at this angle of attack. Furthermore, low velocity air is observed in the wake behind the airfoil (indicated by light blue region).

For the NACA 64-006 airfoil, some similarities and differences were observed in the velocity flow field. The velocity contours for this airfoil can be seen below in Figure 23.

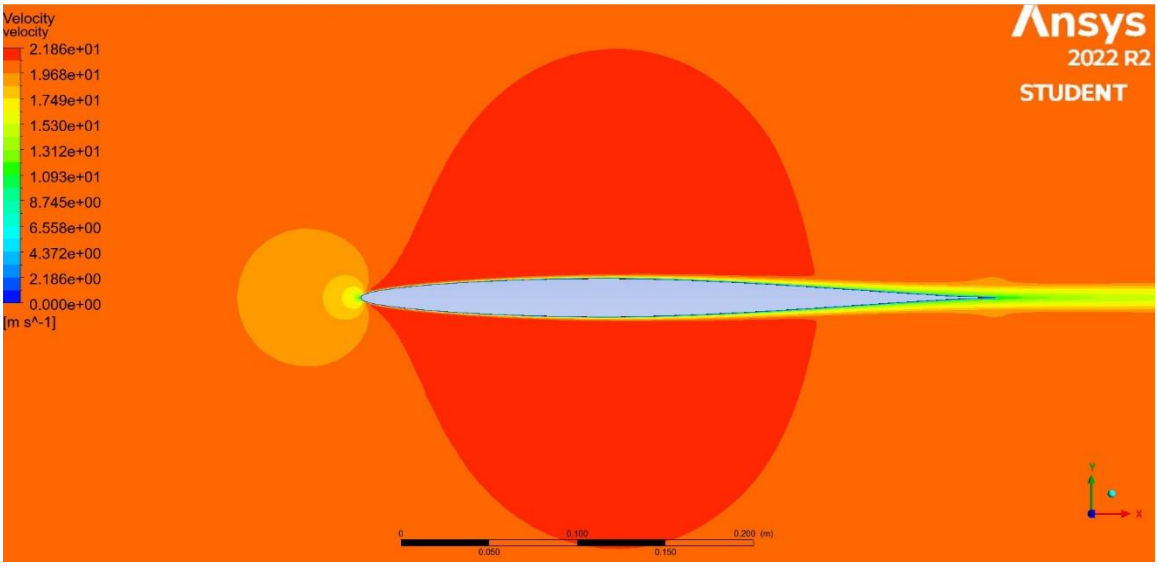

a) NACA 64-006 airfoil, $\alpha = 0°$

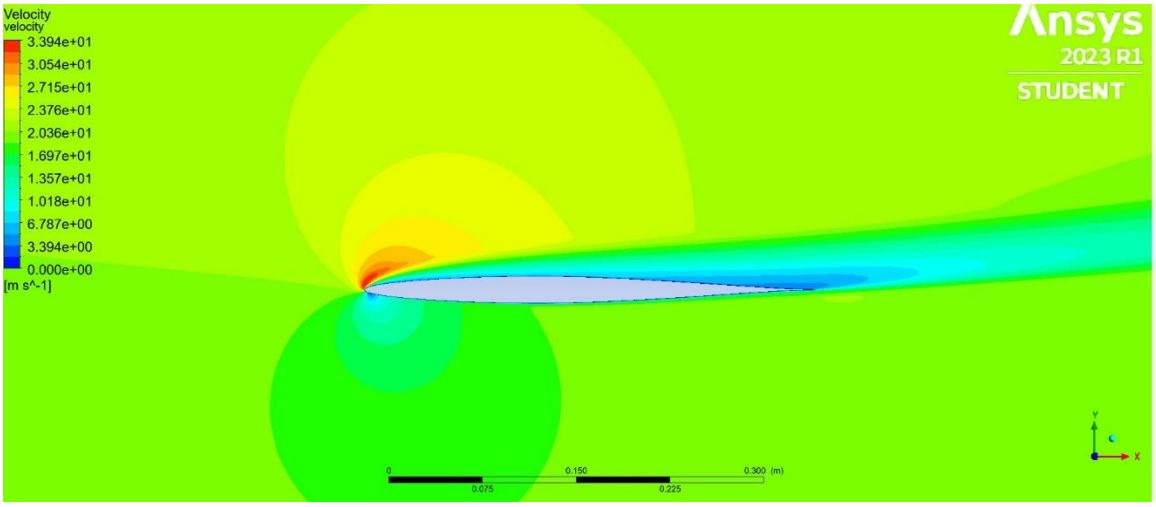

b) NACA 64-006 airfoil, $\alpha = 8°$

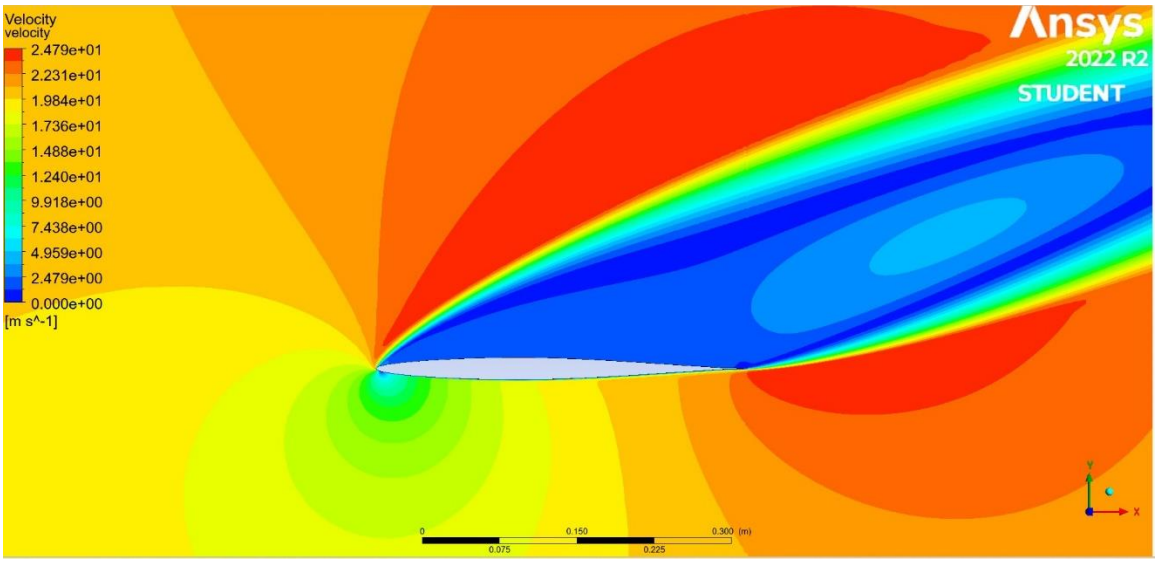

c) NACA 64-006 airfoil, $\alpha = 20°$

Figure 23. NACA 64-006 airfoil velocity flow field at various angles of attack

At $\alpha = 0$ degrees, the velocity in the proximity of the airfoil is different from the freestream velocity. As stated before, this is due to the propagation of disturbances throughout the flow field at subsonic speeds. Directly in front of the leading edge, regions of airflow with a local velocity below the freestream velocity develop (indicated by orange and yellow regions). Due to the streamlined nature of this airfoil, the local velocity of the airflow does not drop significantly near the leading edge. Stagnation points are present at both the leading and trailing edges, where the local velocity is zero (indicated by the blue region). As the air flows over the airfoil, the local velocity rapidly increases (indicated by the red region) and transitions back to the freestream velocity at the trailing edge (indicated by the orange region). This is expected due to the NACA 64-

006 being a high-speed airfoil. Looking at the laminar boundary layer, the velocity near the surface is zero and progressively increases to the freestream velocity at the boundary edge.

As the angle of attack increases, the local velocity of the airflow on the top surface begins to drop. However, on the bottom surface, the airflow slows down and then speeds back up. Furthermore, the stagnation point at the leading edge is observed to move further downstream of the airfoil. At $\alpha = 8$ degrees the boundary layer thickness has increased, which results in lower-speed air covering the surface of the airfoil (indicated by the blue regions). At the edge of the boundary layer, the airflow returns to the freestream velocity (indicated by the green region). At $\alpha = 20$ degrees, the top surface is covered by a large region of low velocity air (indicated in blue), which is characteristic of separated airflow. This region of "dead air" spans the entire chord length of the airfoil and extends into its wake. The airfoil experiences "leading edge stall" at this angle of attack, which is flow detachment at the leading edge. Due to the boundary layer detachment, the wake behind the airfoil is very turbulent, which is characterized by large velocity gradients.

3.1.3 Streamlines

Streamlines help visualize the flow of fluid elements around an aerodynamic body, which can help better understand the boundary layer development and wake

characteristics. The streamline contour for the flat plate delta wing can be seen below in Figure 24.

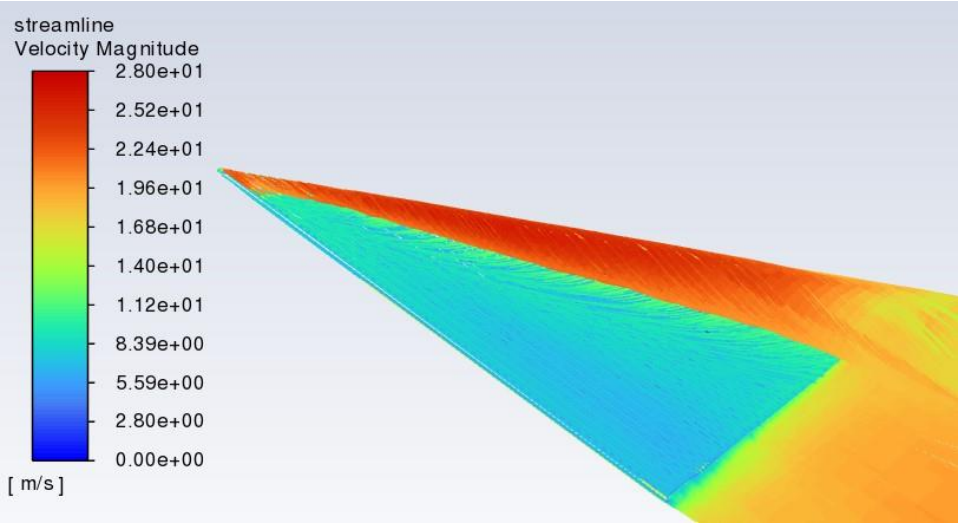

a) Flat plate delta wing, $\alpha = 10°$

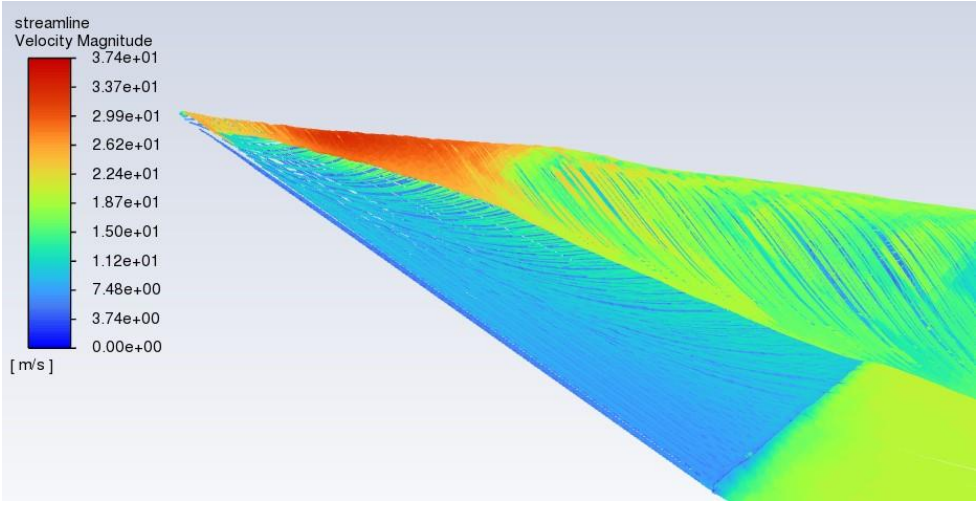

b) Flat plate delta wing, $\alpha = 20°$

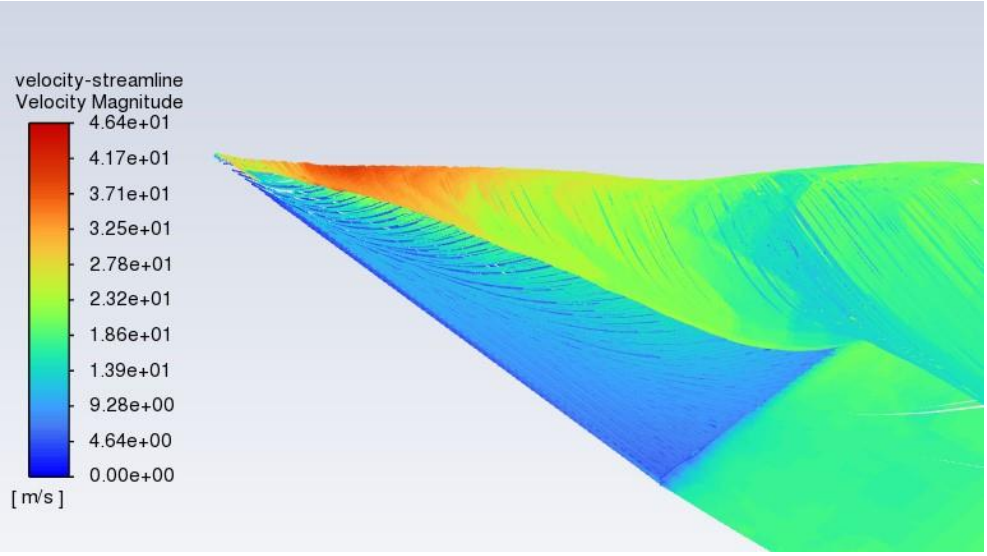

c) Flat plate delta wing, $\alpha = 30°$

Figure 24. Flat plate delta wing velocity streamlines at various angles of attack

At $\alpha = 0$ degrees, the boundary layer on the delta wing is fully laminar and high velocity air moves along the length of the flat plate delta. However, as the angle of attack increases, the leading-edge vortex forms at the leading edge of the wing. A pressure difference between the top and bottom surfaces causes the streamlines on the bottom to curl around the leading edge on to the top. The fully developed vortex is characterized by airflow that is rotating with a very high local velocity. The streamlines directly inboard of the vortex remain attached and continue downstream undisturbed. However, as the angle of attack increases past 15 degrees, vortex breakdown begins.

The type of vortex breakdown observed is called “bubble” vortex breakdown. At $\alpha = 20$ degrees, a portion of the leading-edge vortex is still attached to the wing (near the apex) and the other portion is detached (near the trailing edge). Behind the region where there is high velocity vortical flow (indicated by the red region), a stagnation point in the axial direction has formed (indicated by blue region inside vortex). This results in an oval shape recirculation bubble forming, where the vortical velocity has dropped and the vortex has expanded. This region then transitions into turbulence as it nears the trailing edge. At $\alpha = 30$ degrees, the vortex grows even larger in both the vertical and spanwise direction due to a rise in pressure. Furthermore, only a small portion of the vortex is still stable and attached to the delta wing (near the apex). As the vortex breakdown grows with increasing angle of attack, the turbulent flow grows, and the wing eventually stalls.

These same characteristics can be observed in the simulation results of the XQ-1A full aircraft model. Below are the velocity streamlines for the XQ-1A in Figure 25 and Figure 26.

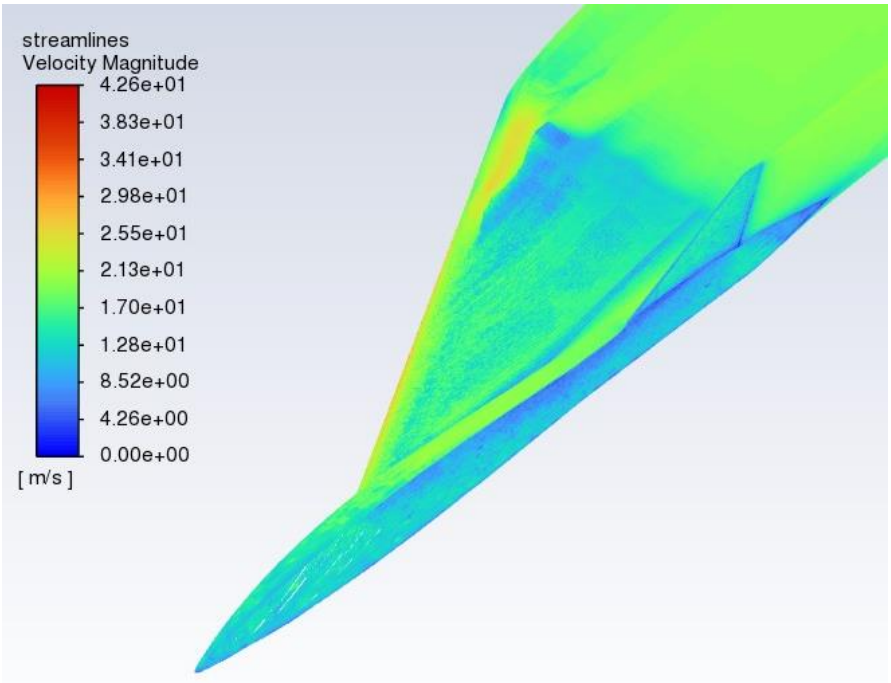

a) XQ-1A, $\alpha = 10°$

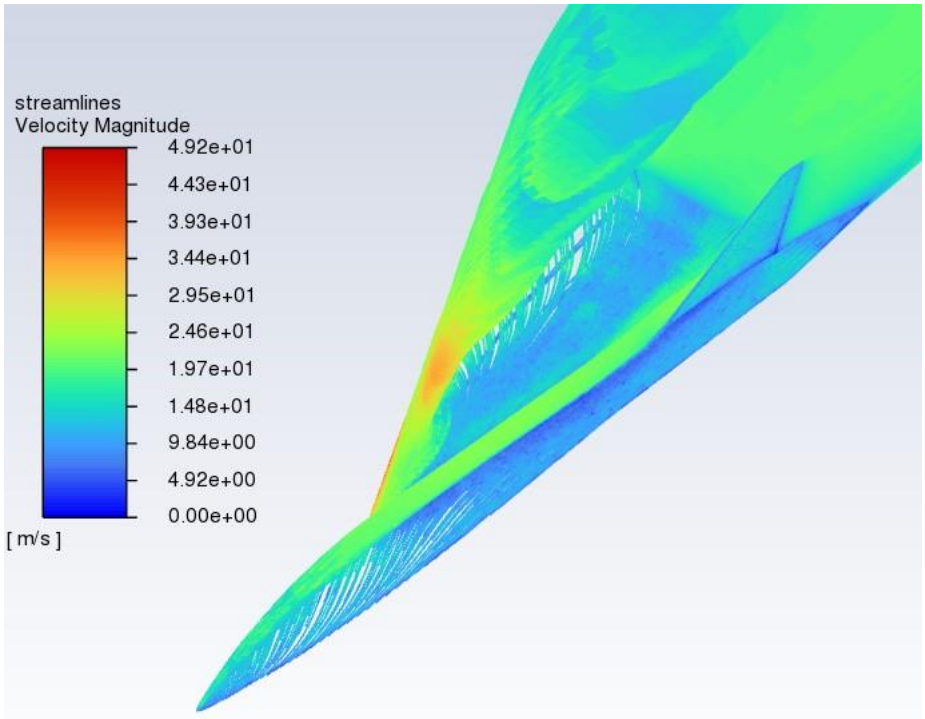

b) XQ-1A, $\alpha = 20°$

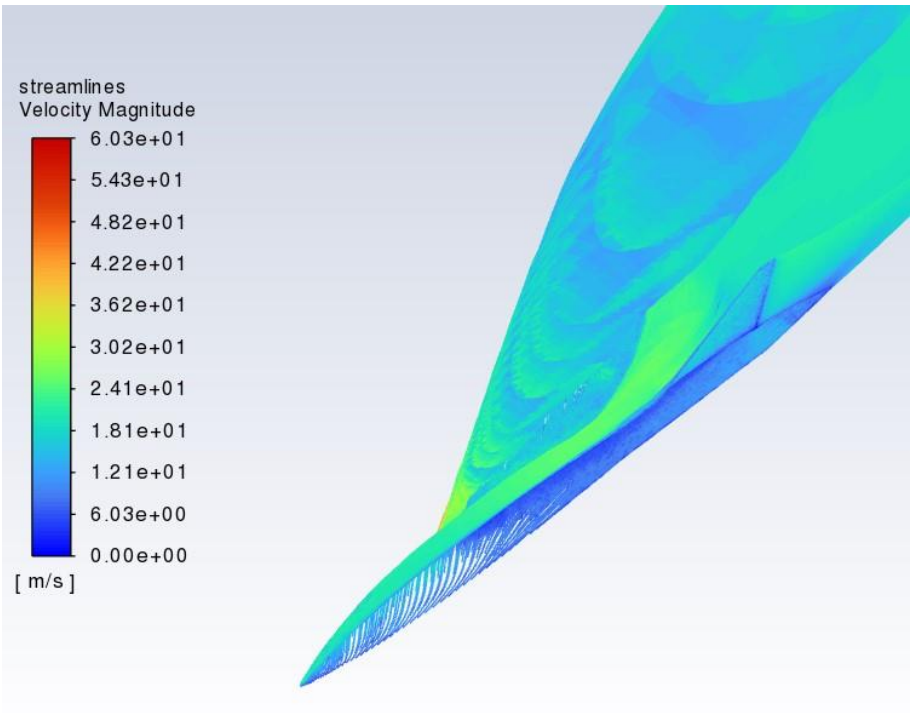

c) XQ-1A, $\alpha = 30°$

Figure 25. Isometric view of XQ-1A velocity streamlines at various angles of attack

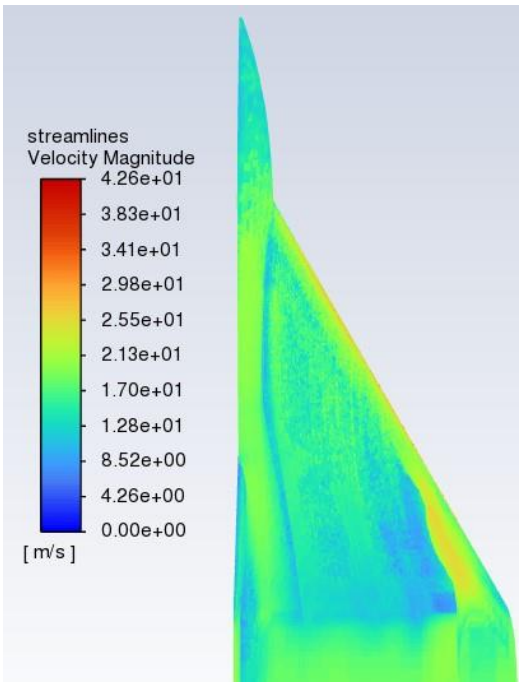

a) XQ-1A, $\alpha = 10°$

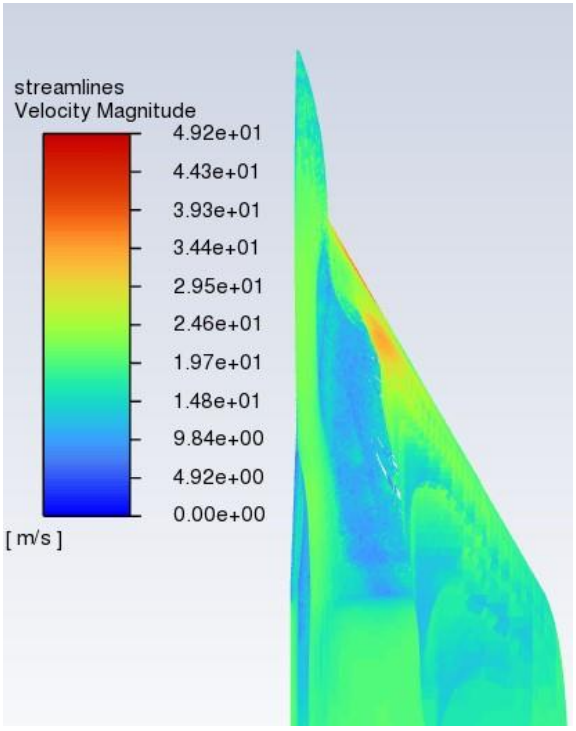

b) XQ-1A, $\alpha = 20°$

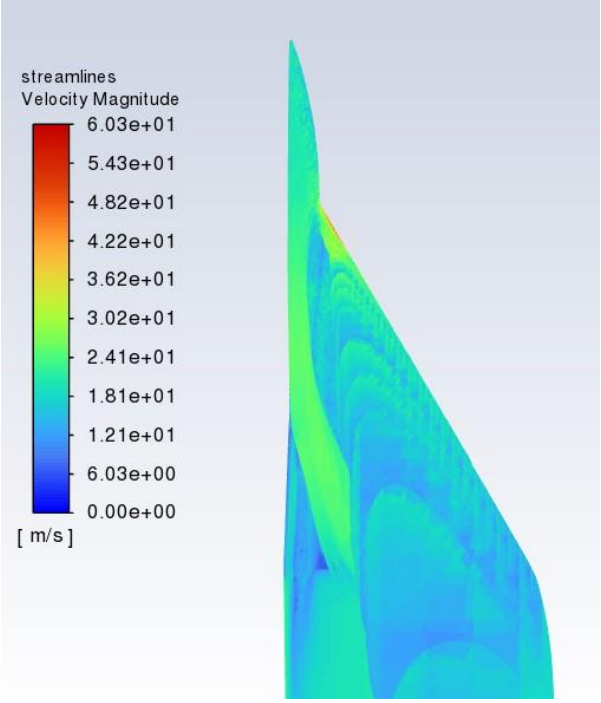

c) XQ-1A, $\alpha = 30°$

Figure 26. Top view of XQ-1A velocity streamlines at various angles of attack

At $\alpha = 0$ degrees, the boundary layer across the XQ-1A is fully laminar and local high velocity air moves over the wing and fuselage. However, as the angle of attack increases, the leading-edge vortex forms inboard of the leading edge. At $\alpha = 10$ degrees, the leading-edge vortex does not fully develop like on the flat plate delta wing. This is most likely due to the introduction of the fuselage of the aircraft, which causes an alteration of the flow field over the delta wing. Furthermore, the local velocity of the air in the vortex (indicated by yellow and light red regions) is not as high as in the vortex for the flat plate

delta wing. The streamlines directly inboard of the developing leading-edge vortex continue downstream unaffected. However, streamlines closer to the wing-root move in a non-linear pattern compared to the streamlines near the wing-root of the flat plate delta. This is due to the nature of the fuselages shape.

As the angle of attack increases to 20 and 30 degrees, the leading-edge vortex begins to breakdown and the flow over the wing becomes more turbulent. Like the flat plate delta wing, “bubble” type vortex breakdown occurs. However, some key differences are apparent. At $\alpha = 20$ degrees, the oval recirculation region behind the stagnation point is smaller and only a small portion of the vortex is still attached. For the flat plate delta, the recirculation region was longer and more of the vortex was still attached. The local velocity in the stable portion of the vortex (indicated by yellow and light red regions) is less than it was for the flat plate delta at this angle of attack. At $\alpha = 30$ degrees, the vortex breakdown has grown even further. The unstable portion of the vortex has expanded further in the vertical and spanwise direction. The air flow in the unstable portion is less than the velocity in the stable portion. Only a smaller portion of the stable vortex remains attached to the wing. As the angle of attack increases further, the vortex breakdown will progress until the vortex has fully decayed, resulting in the aircraft stalling.

3.2 Model Validation and Verification

Model validation and verification is an important process that ensures CFD models are accurately modeling the flow physics and provide results that are accurate. In this section, the model validation and verification process will be discussed. This process involved comparing simulated results with experimental data collected by the FVDT and theoretical data obtained from the leading-edge suction analogy. In the proceeding sections, a description of the leading-edge suction analogy will be given first. Next, the experimental data collection process will be detailed, specifically what facilities and equipment were used. Finally, the simulated results will be discussed. During this discussion, important aerodynamic parameters and trends observed in the subsequent lift curves, drag polars, and aerodynamic efficiency plots will be covered.

3.2.1 Leading Edge Suction Analogy

Developed by Edward C. Polhamus [17,18], the leading-edge suction analogy is an important analytical method utilized to predict subsonic lift and drag characteristics for various delta wing planforms. This theory can be applied to wings that have no camber, twist, and are sufficiently thin enough. Furthermore, it is assumed that the leading edge of the wing is sharp enough to cause the flow to separate at the leading edge and no leading-edge suction occurs. The basis of the theory is on the analogy between vortex lift and the leading-edge suction due to potential flow at the leading edge. Since vortex flow induces reattachment and a Kutta condition exists at the trailing edge, it is

assumed the total lift has a potential flow and vortex lift component. The vortex and potential flow lift components can be seen in the lift and drag equations below in equations 12 and 13.

$$C_L = K_p \sin(\alpha) cos^2(\alpha) + K_v \cos(\alpha) sin^2(\alpha) \qquad (12)$$

$$C_D = C_{D_0} + K_p sin^2(\alpha) \cos(\alpha) + K_v sin^2(\alpha) \qquad (13)$$

K_p and K_v are constants associated with the potential flow and vortex lift coefficients respectively. The relationship between these two constants and a wings aspect ratio can be seen below in Figure 27.

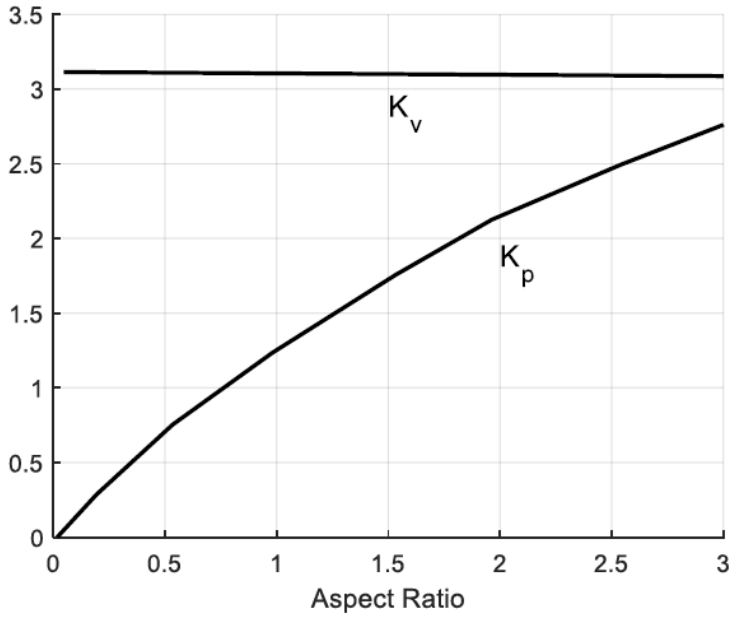

Figure 27. K_p and K_v as a function of aspect ratio [6]

As can be seen in the figure above, K_p rapidly increases with aspect ratio, while K_v appears to be independent of it. Compared to other analytical methods developed previously, the leading-edge suction analogy provides more accurate results across a wide range of delta wings up to angles of attacks of 20 degrees or greater. Furthermore, this analogy can be extended to the supersonic flow regime, where it accurately predicts the reduction in vortex lift with increasing Mach number. This makes it a powerful analytical method to use for validating computational models.

3.2.2 Experimental Data Collection

The experimental data used for validating the flat plate delta wing and XQ-1A full aircraft models were gathered by the Flight Vehicle Design and Testing Group at the ARC. The XQ-1A was tested with both a 60-degree flat plate delta wing and a 60-degree delta wing made from a NACA 64-006 high speed airfoil. The facility utilized was a 3'x5' low speed Eiffel type open circuit subsonic wind tunnel. The wind tunnel has a maximum airspeed of 180 ft/s and a test section area of 39" x 59" x 96". The wind tunnel can be seen below in Figure 28.

Figure 28. External view of 3'x5' wind tunnel at the ARC [6]

Airspeed in the wind tunnel was monitored in real time using LabView. To determine the air speed of the wind tunnel, static pressure and total pressure were measured. To measure the aerodynamic loads on the model an HH-388 six-component internal force balance was used. The XQ-1A was mounted using a sting support system, which was made of a steel parallelogram linkage system. The system was designed in such a way that ensured any vibration induced by unsteady aerodynamic flow would not skew the data. The HH-388 six-component internal force balance can be seen below in Figure 29.

Figure 29. Six component internal force balance [6]

Wind tunnel testing was conducted at a Reynolds number of 5×10^5 based on the wing's mean aerodynamic chord. Lift, drag, and pitching moment data was collected for angles of attack ranging from 0 degrees to 35 degrees. Only the lift and drag coefficient data were utilized to validate the flat plate delta wing and XQ-1A full aircraft models. The experimental data gave valuable insight into each CFD models accuracy, which is crucial for having confidence in making design decisions using these models.

3.2.3 CFD Results

Results from the simulations included lift and drag coefficients and lift and drag forces at various angles of attack. This information was utilized to create lift curves, drag polars, and aerodynamic efficiency plots for each CFD model. Below in Figure 30, the results for the NACA 0012 airfoil are shown.

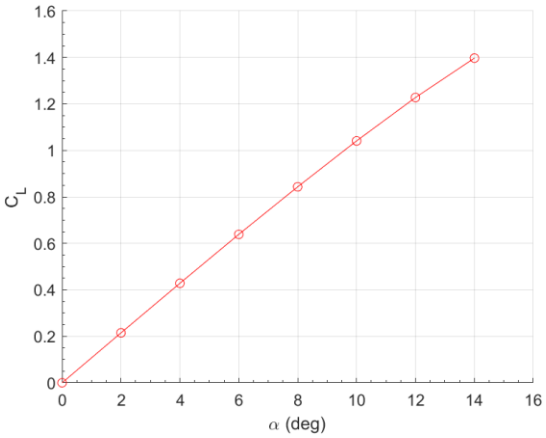

a) Lift Curve

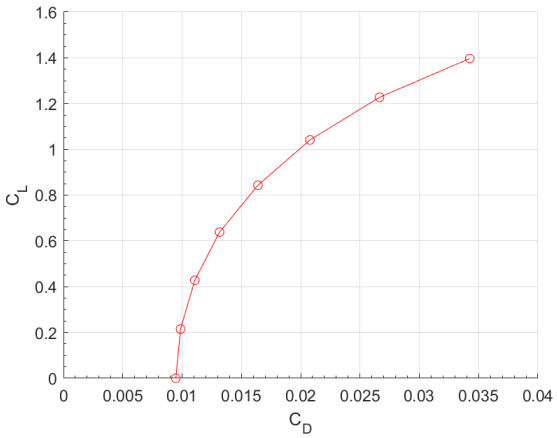

b) Drag Polar

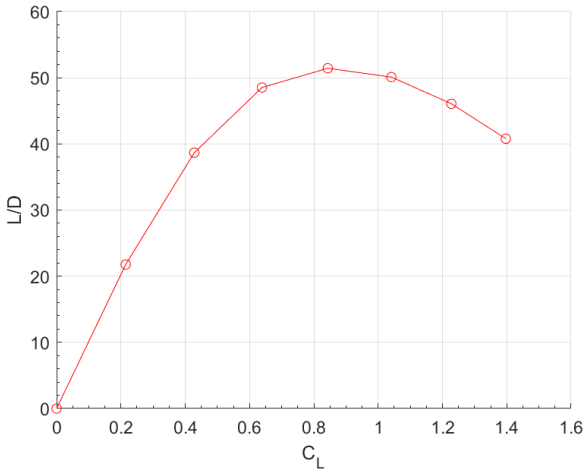

c) Aerodynamic Efficiency

Figure 30. Numerical results for the NACA 0012 airfoil at Re = 3M

At a Reynolds number of 3 million, the lift curve for the NACA 0012 airfoil exhibited a purely linear relationship between lift coefficient and angle of attack. The lift curve slope is 0.1005 per degree, which was deemed appropriate based off experimental data from literature. The maximum coefficient of lift presented here is 1.4 and it occurs at angle of

attack of 14. In this range of angles of attack, the NACA 0012 has yet to stall due to the lack of drop in lift.

In the drag polar, the zero lift drag coefficient is approximately 0.009. This means the airfoil experiences a minimal amount of parasitic drag. As the lift generated by the airfoil increases, the drag increases non-linearly. At a lift coefficient of 1.4, the drag experienced by the airfoil is 0.034. This increase in drag results from the introduction of pressure drag as the angle of attack increases. This will in turn affect the aerodynamic efficiency of the airfoil. The maximum lift-to-drag ratio is approximately 51 and it occurs at a coefficient of lift of 0.8. At higher lift coefficients, the lift-to-drag ratio decreases. This indicates more drag is being generated compared to lift. This is not ideal because large amounts of drag harm the aerodynamic performance of aircraft.

The results for the NACA 64-006 airfoil at a Reynolds number of 500,000 and 3,000,000 can be seen below in Figure 31. First, simulations were conducted at a Reynolds number of 3,000,000 to get results to compare to experimental data from literature.

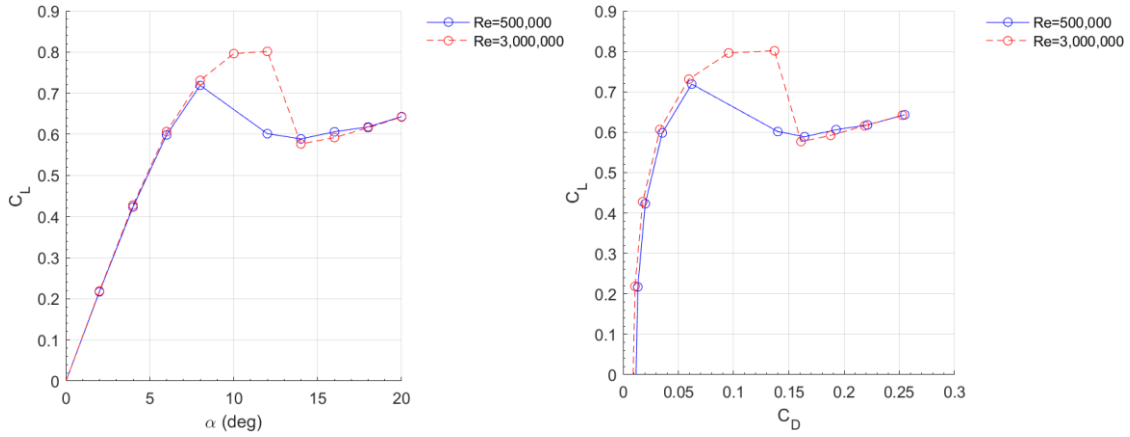

a) Lift Curve b) Drag Polar

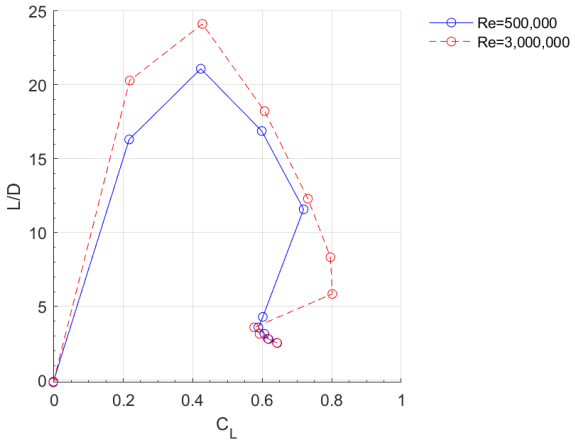

c) Aerodynamic Efficiency

Figure 31. Numerical results for the NACA 64-006 airfoil at Re = 500K and Re = 3M

Doing this first ensured the results produced by the numerical model were accurate. Once achieved, the simulations were run at a Reynolds number of 500,000. At a Reynolds number of 3,000,000, the lift curve slope is approximately 0.1046 per degree, which was appropriate based on data from literature. Likewise, at a Reynolds number of 500,000 the lift curve slope is 0.1046 per degree. The maximum lift coefficient at a Reynolds number of 3,000,000 is 0.8 and occurs at an angle of attack of 10 degrees. Due to convergence issues at an angle of attack of 10 degrees, the max lift coefficient could not be computed at a Reynolds number of 500,000. The 10-degree angle of attack was omitted from the lift curve at a Reynolds number of 500,000. Both lift curves experience a drastic drop in lift after an angle of attack of 10 degrees, indicating the airfoil has stalled. This drastic drop in lift is characteristic of a leading-edge stall. The leading-edge stall is when the

boundary layer separates from the airfoil surface abruptly, with the origin of the separation being the leading edge. Due to the boundary layer separation, the flow along the airfoil surface becomes turbulent and causes an increase in pressure drag.

As seen in the drag polar, the drag experienced by the airfoil at each Reynolds number is similar. The zero lift drag coefficient at both Reynolds number is approximately 0.009. Due to the more streamlined nature of the NACA 64-006 airfoil, the zero-lift drag coefficient is smaller than other airfoils, like the NACA 0012. For a high-speed airfoil like the NACA 64-006, a very low amount of drag is desired. At a Reynolds number of 3,000,000, the drag coefficient at the max lift coefficient is approximately 0.14. After the airfoil has stalled, there is a drop in lift and drag for a brief period before they begin increasing again. This increase in drag results from pressure drag from boundary layer separation at higher angles of attack. We expect the drag values obtained from the simulations to be much higher than observed in real life due to a turbulence model being selected. The NACA 6 series airfoils were designed to maintain laminar flow over a significant amount of the airfoils surface, thus reducing drag.

The aerodynamic efficiency of the NACA 64-006 at each respective Reynolds number varies slightly. At a coefficient of lift of 0.42, the maximum lift-to-drag ratio at a Reynolds number of 3,000,000 is approximately 24, while at a Reynolds number of 500,000 it is approximately 21. This slight difference in aerodynamic efficiency indicates that the NACA 64-006 is more aerodynamically efficient at higher Reynolds numbers than at lower Reynolds numbers. This makes sense due to how the NACA 64-006 airfoil has been designed. As the lift generated by the airfoil increases, the aerodynamic

efficiency at both Reynolds numbers drops dramatically. This dramatic drop indicates that there is significantly more drag being generated than lift. For highly maneuverable aircraft using this airfoil, this will have direct impacts on the rate of climb, range, and endurance of the aircraft.

The results for the flat plate delta wing at a Reynolds number of 500,000 can be seen below in Figure 32. Simulated results were compared with experimental data and theoretical data obtained from the leading-edge suction analogy.

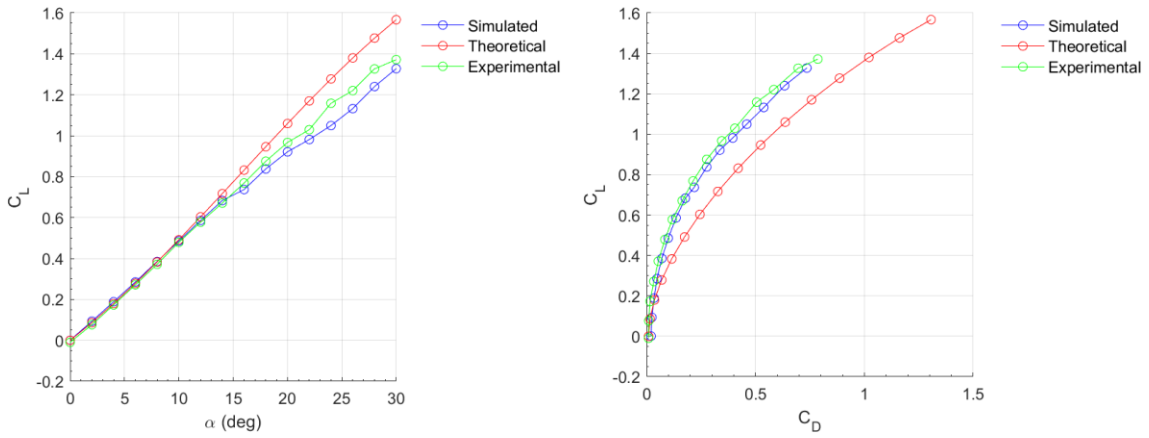

a) Lift Curve

b) Drag Polar

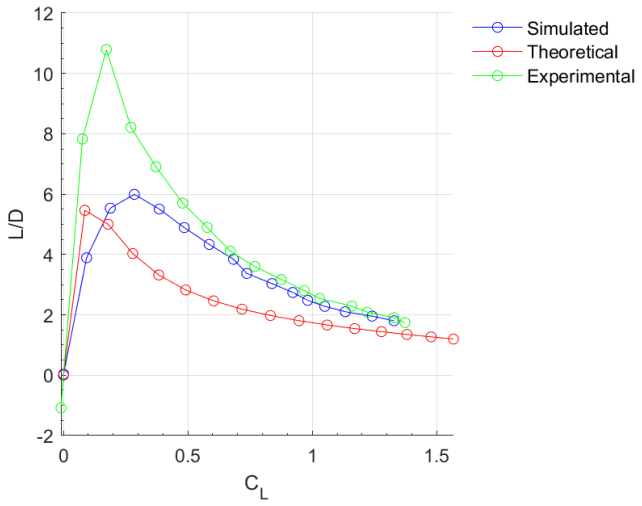

c) Aerodynamic Efficiency

Figure 32. Numerical results for a flat plate delta wing at a Re = 500K

The universal trend between the three lift curves is that their lift curve slopes are similar. The simulated lift curve has a lift slope of 0.0436 per degree, while the theoretical and experimental lift curves have lift slopes of 0.0539 per degree and 0.0474 per degree respectively. The percent error between the simulated and theoretical lift curve slopes is 19.1520%. On the other hand, the percent error between the simulated and experimental lift curve slopes is 8.1927%. The percent error between the simulated and theoretical lift curve slopes is greater than the percent error between the simulated and experimental. This can be attributed to certain assumptions that are made by the theory, which result in the lift curve of the delta wing being higher than observed. Furthermore, the element size of cells in the mesh would affect the results. A more refined mesh would yield more accurate results due to the complex flow features of the delta wing getting captured

better. Due to the cell count limitations of the student version of Ansys FLUENT, a more refined mesh wasn't possible.

All three lift curves align with each other between angles of attack of 0 and 14 degrees. However, after 15 degrees the lift curves begin to diverge from each other. After 15 degrees, the simulated results follow the experimental results better than the theoretical results. In this range of angles of attack, the maximum coefficient of lift from the simulated results is about 1.32 at an angle of attack of 30 degrees. At the same angle of attack, both theoretical and experimental results observed an even higher maximum lift coefficient. Due to the leading-edge vortex, the delta wing generates a large amount of lift. Furthermore, the delta wing has not stalled in this range of angles of attack like other wing configurations would.

The drag polar showed similar trends, which revealed the simulated results followed the experimental results well. The zero-lift drag coefficient for the flat plate delta wing from the simulated results is 0.020552. In comparison, the zero lift drag coefficient for both the theoretical and experimental results is approximately 0.009. These differences are due to CFD's struggles with making accurate drag predictions. As the lift increases, the skin friction drag experienced by the delta wing begins to transition to pressure drag due to flow separation and vortex breakdown. This results in a significant increase in the drag coefficient. Compared to theory, simulated and experimental results predicted less drag for the delta wing at higher lift coefficients.

The aerodynamic efficiency of the delta wing exhibited some interesting trends. The simulated results reported a max lift-to-drag ratio of 6 at a lift coefficient of

approximately 0.28. On the other hand, theory predicted a max lift-to-drag ratio of 5.4 at a lift coefficient of 0.08. In comparison, experimental data reported a maximum lift-to-drag ratio of 10.7 at a lift coefficient of approximately 0.17. Both simulated and theoretical results predicted lower aerodynamic efficiency for the flat plate delta wing than experimental results. These differences again could be attributed to assumptions made by theory and the mesh used in FLUENT. In general, the maximum lift-to-drag ratio is considerably less compared to other conventional wing configurations.

Similar results were observed in the simulations for the XQ-1A. Results from these simulations at a Reynolds number of 500,000 can be seen below in Figure 33.

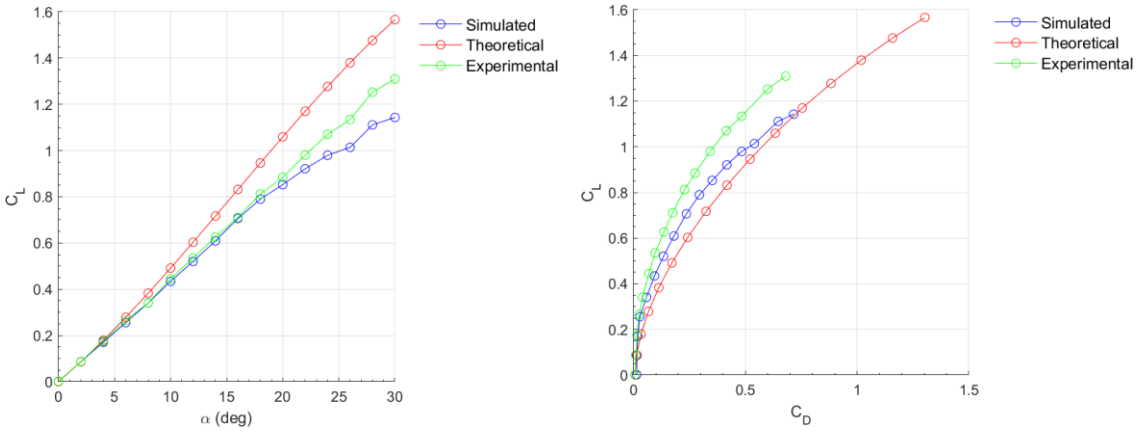

a) Lift Curve b) Drag Polar

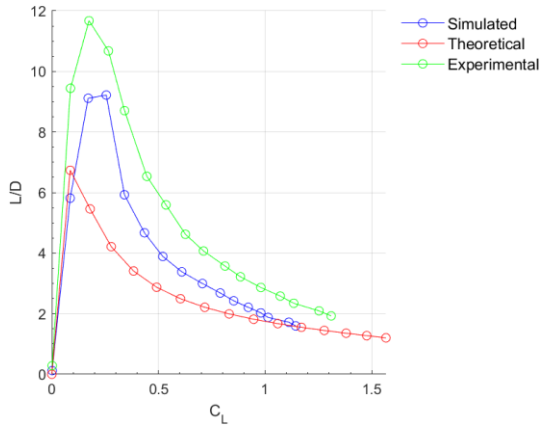

c) Aerodynamic Efficiency

Figure 33. Numerical Results for the XQ-1A at a Re=500K

The lift curves exhibited lift slopes that were close to each other. The simulated results had a lift curve slope of 0.0392 per degree, while theory and experimental results had a lift curve slope of 0.0539 per degree and 0.0442 per degree respectively. The percent error between the simulated and theoretical lift curve slopes is 27.2307%, while the percent error between the simulated and experimental lift curve slopes is 11.3815%. This increase in error compared to the flat plate delta wing is due to a less refined mesh. The cell limitations of the student version of Ansys FLUENT resulted in a less optimal mesh for the XQ-1A's complex geometry. With a more refined mesh, more accurate results could have been obtained.

The simulated results followed the experimental results more closely than the theoretical results. From angles of attack between 0 and 18 degrees, the simulated results aligned well with the experimental results. However, after 18 degrees the results begin to

diverge from each other. At higher angles of attack, flow separation and vortex breakdown become difficult to model with a less refined mesh. The accuracy of the results decreased due to the complex nature of the flow. In this range of angles of attack, the maximum lift coefficient is approximately 1.14. On the other hand, the maximum lift coefficient for the theoretical and experimental results is approximately 1.56 and 1.30 respectively. The simulated results predicted a lift coefficient that was far less than expected at this angle of attack for delta-winged aircraft.

The drag polar for the XQ-1A and flat plate delta wing showed various similarities. However, the simulated results tended to follow the theoretical results more for the XQ-1A. At similar coefficients of lift, simulated and theoretical results predicted higher drag values compared to experimental results. The simulated zero-lift-drag coefficient for the XQ-1A is 0.0135. In contrast, the zero-lift drag coefficient for both the experimental and theoretical results is approximately 0.006. CFD does not always give accurate drag results for various reasons, such as mesh quality and assumptions made by the model. The aerodynamic efficiency of the XQ-1A appears to be slightly greater than that of the flat plate delta wing. The simulated results had a maximum lift-to-drag ratio of approximately 9, while theoretical and experimental results predicted a maximum lift-to-drag ratio of approximately 6.7 and 11.6. This difference in aerodynamic efficiency can be attributed to differences in the type of delta wing used. The delta wing used by the XQ-1A utilizes a NACA 64-006 airfoil, which has a shape that minimizes drag. On the other hand, the flat plate delta wing doesn’t use this airfoil. The improved aerodynamic efficiency of the XQ-1A with this type of delta wing configuration means it will excel in

different areas of performance compared to the flat plate delta wing configuration. Performance areas where it'd be superior would be the rate of climb, range, endurance, and speed.

Chapter 4. Conclusions

4.1 Summary

With the growing use of UAVs in the United States and abroad, there is a rising need for UAVs to fulfill roles in the military that require high maneuverability and survivability. This makes it imperative for more research to be done into UAV technology and the application of high-speed wing configurations to their design. The delta wing is a unique high-speed wing configuration that can provide UAVs with increased maneuverability. At low speeds and high angles of attack, the leading-edge vortex generates more lift compared to conventional wing configurations. This thesis focused on studying the low-speed aerodynamics of a 60-degree delta wing using CFD. The primary motivation of this research was to help the Flight Vehicle Design and Testing Group make future design enhancements to the XQ-1A UAV.

To perform CFD simulations, the student version of Ansys FLUENT was used. The NACA 0012 and NACA 64-006 airfoils, along with a flat plate delta wing and XQ-1A, were studied using CFD. A critical step in the CFD model development process was fluid domain generation and meshing. Mesh generation involved selecting the type of cells, mesh (structured or unstructured), boundary layer mesh, quality metrics, and y-plus value. Due to simulation conditions, flow separation at high angles of attack, and vortex

breakdown, turbulence modeling was deemed appropriate. The turbulence model selected was the Realizable $k - \varepsilon$ model. Boundary conditions for each model were discussed, such as inlet, outlet, symmetry, and wall.

Simulations conditions for the NACA 0012 model were a Reynolds number of 3,000,000 and standard day conditions. For the NACA 64-006 model, simulation conditions were Reynolds numbers of 500,000 and 3,000,000 and standard day conditions. For the flat plate delta wing and XQ-1A, simulation conditions were at a Reynolds number of 500,000 and standard day conditions. Flow field visualizations were created for each model using pressure contours, velocity contours, and streamline contours. Pressure contours for the airfoils revealed that as angle of attack increases, the pressure varies across the airfoils and flow separates. For the delta wing models, the pressure contours revealed the leading-edge vortex resulted in low pressure regions inboard of the leading edge. Velocity contours revealed that the local velocity of the airflow is higher in the proximity of the airfoil than the freestream. Furthermore, "dead air" forms along the airfoil surface when flow had separated. Streamline contours revealed that the vortex has high velocity vortical flow, and vortex breakdown occurs with increasing angle of attack. The type of vortex breakdown observed for both delta wing models was bubble type.

Simulation results for each model aligned well with experimental and theoretical data. The NACA 0012 and NACA 64-006 models were validated using data from literature. The simulated lift curve slope for the NACA 0012 at a Reynolds number of 3,000,000 was 0.1005 per degree. The simulated lift curve slope for the NACA 64-006

airfoil at a Reynolds number of 500,000 and 3,000,000 was 0.1046 per degree. The flat plate delta wing and XQ-1A models were validated using experimental data gathered by the FVDT and Polhamus's leading edge suction analogy. The simulated results for the flat plate delta wing had a lift curve slope of 0.0436 per degree. The percent error between the simulated and experimental lift curve slopes was 8.1927%, while the percent error between the simulated and theoretical lift curve slopes was 19.1520%. The simulated results for the XQ-1A had a lift curve slope of 0.0392 per degree. The percent error between the simulated and experimental lift curve slopes was 11.3815%, while the percent error between the simulated and theoretical lift curve slopes was 27.2307%.

Due to the limitations of the student version of Ansys FLUENT, the complexity of the model, and available computing resources, the results from the delta wing models were deemed reasonable. A more refined mesh would yield more accurate results. However, this would come at the cost of increasing computational time. At higher angles of attack, the accuracy of the simulated lift coefficients for the XQ-1A decreased. This is due to the complex flow features that develop at high angles of attack being more complicated to model with a coarser mesh. However, the mesh generated for the NACA 0012, NACA 64-006, and the flat plate delta wing produced results that aligned well with both experimental and theoretical data. Without a cell count limitation and access to appropriate computing power, CFD is a very powerful tool in the aircraft design process. This research has demonstrated the capability of CFD to simulate aircraft designs under various conditions to understand their aerodynamic performance.

4.2 Future Work

Using the baseline model for the XQ-1A developed in FLUENT, it can be modified to include other high-speed wing configurations. High-speed wing configurations that could be studied include the double delta wing, ogive wing, and diamond wing. The information gathered from these simulations could give the FVDT valuable insight into the aerodynamic performance of the XQ-1A with each of these wing configurations. This would help with making future design improvements to the novel aircraft design.

Furthermore, simulating the baseline wing configuration with articulated wingtips could be done in FLUENT. The FVDT has researched how articulated wing tips effect the leading-edge vortex structures that develop on a delta wings. This model could give additional insights into the aerodynamic impacts of articulated wingtips on the leading-edge vortex and the XQ-1A's overall performance. After validating the model with theoretical and experimental data, other high speed wing configurations with articulating wing tips can be studied. This would provide an understanding about the impact articulated wingtips have on other high speed wing configurations at low speeds. Each wing configurations performance with articulated wing tips could be compared to identify the optimal design.

References

[1] J. Gertler, U.S Unmanned Aerial Systems, https://crsreports.congress.gov/product/details?prodcode=R42136.

[2] J. R. Hoehn, K. M. Sayler, and M. E. DeVine, Unmanned Aircraft Systems: Roles, Missions, and Future concepts, https://crsreports.congress.gov/product/pdf/R/R47188.

[3] Task Force on Unmanned Aerial Vehicles and Uninhabited Combat Aerial Vehicles., Washington, D.C.: Office of the Under Secretary of Defense for Acquisition, Technology, and Logistics, 2004.

[4] W. B. Herbst, "Dynamics of Air Combat," *Journal of Aircraft*, vol. 20, no. 7, pp. 594–598, 1983. doi:10.2514/3.44916

[5] J. Anderson, *Fundamentals of Aerodynamics*, 6th ed. Mcgraw-Hill, 2016.

[6] Trussa, C. W. "Low-Speed Aerodynamic Characteristics of a Delta Wing with Articulated Wing Tips", 2020, The Ohio State University Master's Thesis.

[7] F. M. Payne and R. C. Nelson, "An Experimental Investigation of Vortex Breakdown on a Delta Wing - NASA Technical Reports Server (NTRS)," NASA, https://ntrs.nasa.gov/citations/19860017724.

[8] I. Gursul, "Recent developments in Delta Wing Aerodynamics," *The Aeronautical Journal*, vol. 108, no. 1087, pp. 437–452, 2004. doi:10.1017/s0001924000000269

[9] B. Pamadi, D. Rao, and T. Niranjana, "Wing Rock and Roll Attractor of Delta Wings at high angles of attack," *32nd Aerospace Sciences Meeting and Exhibit*, 1994. doi:10.2514/6.1994-807

[10] "What is CFD: What is Computational Fluid Dynamics?," SimScale, https://www.simscale.com/docs/simwiki/cfd-computational-fluid-dynamics/what-is-cfd-computational-fluid-dynamics/ (accessed Dec. 16, 2023).

[11] Ansys fluent 12.0 theory guide, https://www.afs.enea.it/project/neptunius/docs/fluent/html/th/node1.htm (accessed Dec. 17, 2023).

[12] Gestione, “CFD Computational Domain,” IdealSimulations, https://www.idealsimulations.com/resources/cfd-computational-domain/ (accessed Dec. 22, 2023).

[13] “What is a mesh?: SimWiki documentation,” SimScale, https://www.simscale.com/docs/simwiki/preprocessing/what-is-a-mesh/#:~:text=Unstructured%20meshes%20are%20more%20general%20and%20can%20arbitrarily,matrix%20or%20list%20and%20the%20node%20coordinates%20list. (accessed Dec. 23, 2023).

[14] Jousefm, “What is Y+ (yplus)?,” SimScale CAE Forum, https://www.simscale.com/forum/t/what-is-y-yplus/82394 (accessed Dec. 23, 2023).

[15] “K-epsilon turbulence model: Global settings,” SimScale, https://www.simscale.com/docs/simulation-setup/global-settings/k-epsilon/ (accessed Dec. 26, 2023).

[16] A thorough description of how wall functions are implemented ... - chalmers, https://www.tfd.chalmers.se/~hani/kurser/OS_CFD_2016/FangqingLiu/openfoamFinal.pdf (accessed Dec. 26, 2023).

[17] Polhamus, E. C., “A Concept of the Vortex Lift of Sharp-Edge Delta Wings Based on a Leading-Edge-Suction Analogy.” NASA Technical Note D-3767, December 1966.

[18] Polhamus, E. C., “Predictions of vortex-lift characteristics by a leading-edge suction analogy.” *Journal of aircraft*, Vol. 8, No. 4, 1971, pp. 193-199. doi: 10.2414/3.44254.

Appendix A. Additional CFD Contours

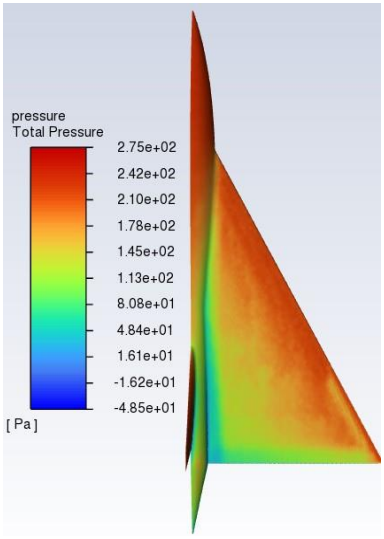

Figure 34. XQ-1A top surface pressure distribution, $\alpha = 0°$

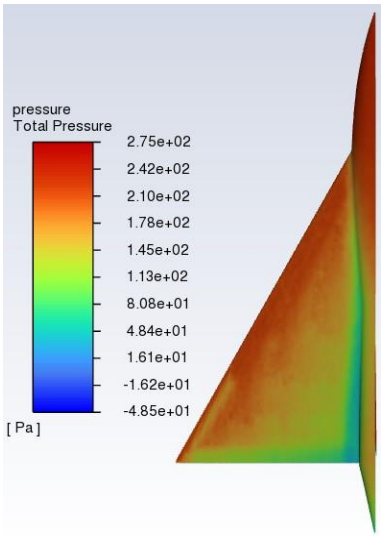

Figure 35. XQ-1A bottom surface pressure distribution, $\alpha = 0°$

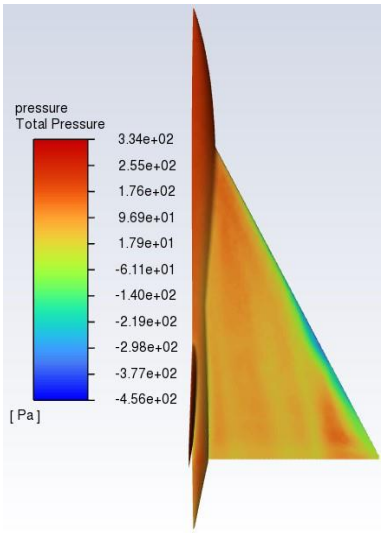

Figure 36. XQ-1A Top surface pressure distribution, $\alpha = 10°$

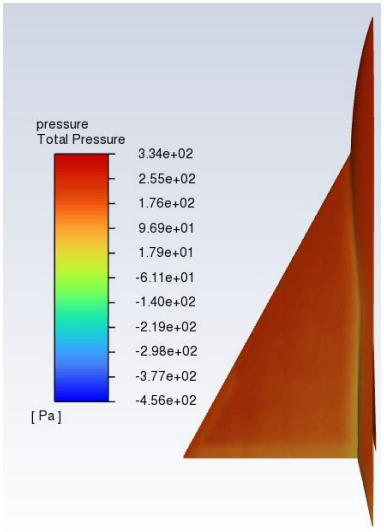

Figure 37. XQ-1A bottom surface pressure distribution, $\alpha = 10°$

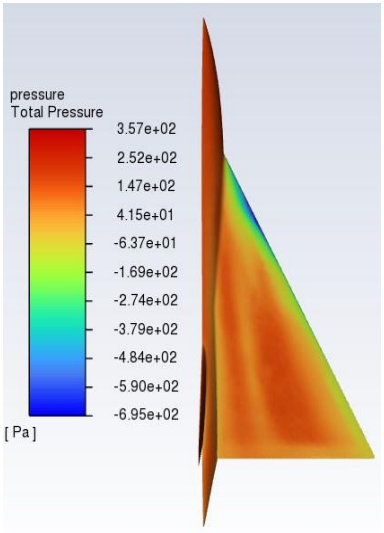

Figure 38. XQ-1A top surface distribution, $\alpha = 20°$

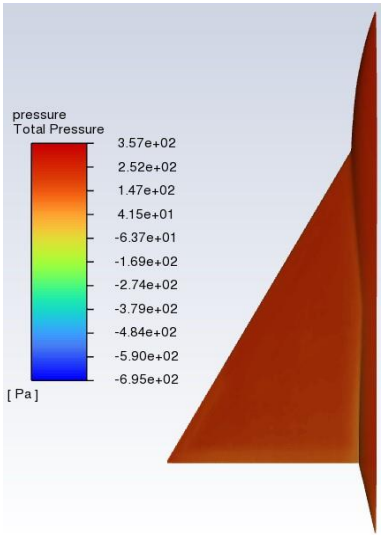

Figure 39. XQ-1A bottom surface distribution, $\alpha = 20°$

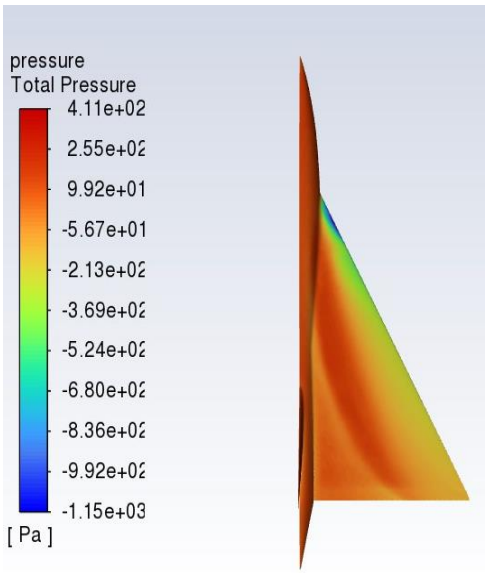

Figure 40. XQ-1A top surface pressure distribution, $\alpha = 30°$

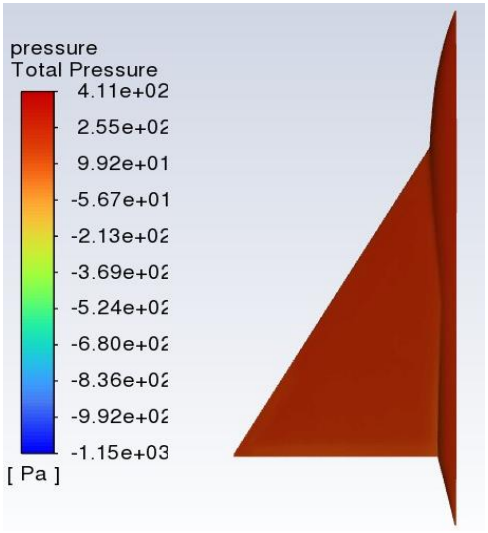

Figure 41. XQ-1A bottom surface pressure distribution, $\alpha = 30°$